RADIATION ENVIRONMENT PREDICTIONS FOR THE IMECE SATELLITE
AND G4BEAMLINE SIMULATIONS FOR THE METU-DBL PROJECT

A THESIS SUBMITTED TO
THE GRADUATE SCHOOL OF NATURAL AND APPLIED SCIENCES
OF
MIDDLE EAST TECHNICAL UNIVERSITY

MERVE YİĞİTOĞLU

IN PARTIAL FULFILLMENT OF THE REQUIREMENTS
FOR
THE DEGREE OF MASTER OF SCIENCE
IN
PHYSICS

FEBRUARY 2017

Approval of the thesis:

RADIATION ENVIRONMENT PREDICTIONS FOR THE IMECE SATELLITE AND G4BEAMLINE SIMULATIONS FOR THE METU-DBL PROJECT

submitted by **MERVE YİĞİTOĞLU** in partial fulfillment of the requirements for the degree of **Master of Science in Physics Department, Middle East Technical University** by,

Prof. Dr. Gülbin Dural Ünver
Dean, Graduate School of **Natural and Applied Sciences** _____

Prof. Dr. Sadi Turgut
Head of Department, **Physics** _____

Assoc. Prof. Dr. Melahat Bilge Demirköz
Supervisor, **Physics Department, METU** _____

Examining Committee Members:

Assoc. Prof. Dr. İsmail Turan
Physics Department, METU _____

Assoc. Prof. Dr. Melahat Bilge Demirköz
Physics Department, METU _____

Prof. Dr. Feza Arıkan
Electrical and Electronics Engineering Department, HU _____

Prof. Dr. Ali Ulvi Yılmazer
Physics Engineering Department, AU _____

Assis. Prof. Dr. Sezer Özerinç
Mechanical Engineering Department, METU _____

Date: _____

I hereby declare that all information in this document has been obtained and presented in accordance with academic rules and ethical conduct. I also declare that, as required by these rules and conduct, I have fully cited and referenced all material and results that are not original to this work.

Name, Last Name: MERVE YİĞİTOĞLU

Signature   :

ABSTRACT

RADIATION ENVIRONMENT PREDICTIONS FOR THE IMECE SATELLITE
AND G4BEAMLINE SIMULATIONS FOR THE METU-DBL PROJECT

Yiğitoğlu, Merve

M.S., Department of Physics

Supervisor   : Assoc. Prof. Dr. Melahat Bilge Demirköz

February 2017, 86 pages

IMECE Satellite will be an Earth observation satellite in Low Earth Orbit (LEO) planned for launch after 2020. Electronic components of the IMECE Satellite will be exposed to a radiation environment in its orbit in space which consists mostly of relativistic charged particles. This radiation environment which can affect the performance and reliability of sensitive materials and electronics is studied using the SPENVIS program. After simulating the space radiation environment, sensitive electronic components and materials intended for space use must be tested to qualify as radiation tolerant components. Radiation effects can be categorized in three groups; Single Event Effects (SEE), Total Ionizing Dose (TID) and Non-Ionizing Dose Displacement Damage Effects. Currently, TID tests can be, but SEE tests cannot be conducted in Turkey. To perform SEE tests, a beam line is being constructed in the R&D room of the Turkish Atomic Energy Agency (TAEA) Sarayköy Nuclear Research and Training Center (SANAEM) Proton Accelerator Facility (PAF). The beam line will provide a final beam profile and energy that will satisfy the requirements of

the ESA-ESCC No:25100 standard. To obtain a beam with the desired parameters, quadrupole magnets and collimators after scattering foils are employed. The radiation dose, received by various beamline elements, environment in the R&D room and especially the target area has been studied with a G4beamline simulation in detail in this thesis. Also, a preliminary study to perform radiation tests at the radiation doses relevant for nuclear reactors is presented.

Keywords: IMECE, Space Radiation Environment, Beamline Simulations, Cosmic Rays

ÖZ

İMECE UYDUSU İÇİN RADYASYON ORTAMI TAHMİNLERİ VE ODTÜ-SDH PROJESİ İÇİN YAPILAN G4BEAMLINE SİMÜLASYON ÇALIŞMALARI

Yiğitoğlu, Merve

Yüksek Lisans, Fizik Bölümü

Tez Yöneticisi   : Assoc. Prof. Dr. Melahat Bilge Demirköz

Şubat 2017 , 86 sayfa

İMECE uydusu Alçak Dünya Yörüngesinde (ADY) yer gözlem uydusu olarak 2020'den sonra görev yapacaktır. İMECE uydusunun elektronik bileşenleri yörüngesinde relativistik yüklü parçacıklara maruz kalacaktır. Hassas elektronik bileşenlerin ve malzemelerin başarısını ve güvenilirliğini etkileyebilecek olan radyasyon ortamı SPEN-VIS programı kullanılarak çalışılmıştır. Uzay ortamının benzetimleri yapıldıktan sonra, uzayda kullanılması planlanan hassas elektronik bileşenlerin ve malzemelerin radyasyona dayanıklı olarak nitelendirilebilmesi için test edilmeleri gerekmektedir. Radyasyon etkileri üç gurupta toplanabilir; Tekil Olay Etkileri (SEE), Toplam İyonize Doz Etkileri (TID) ve İyonize Olmamış Doz Etkiyen Yer Değiştirme Hasarı Etkileri. Günümüzde TID testleri Türkiye'de gerçekleştirilebilirken, SEE testleri henüz gerçekleştirilememektedir. Milli uydu projelerinden doğan ihtiyaç sebebi ile SEE testlerini gerçekleştirebilmek için Türkiye Atom Enerji Kurumu (TAEK)'nun Proton Hızlandırıcı Tesisi (PHT)'nde yer alan Ar&Ge odasında bir demet hattı kurulmaktadır. Ku-

rulan demet hattı, hedef bölgesinde ESA-ESCC No:25100 standardı'na uygun bir demet sağlayacaktır. Gerekli parametrelere sahip bir demeti elde etmek için dört kutuplu mıknatıslar ve saçılmalı folyolardan sonra kolimatörler kullanılmıştır. Bu tezde, Ar&Ge odasındaki çeşitli demet elemanlarından gelen radyasyon doz ortamı ve özellikle hedef bölgesi, G4beamline benzetim programı kullanılarak dataylı olarak çalışılmıştır. Ayrıca nükleer reaktördeki radyasyon ortamına benzer radyasyon testleri yapabilmek için bir demet hattı ön tasarımı yapılmıştır.

Anahtar Kelimeler: İMECE, Uzay Radyasyon Ortamı, Demet Hattı Benzetimi, Kozmik Işınlar

To my family

ACKNOWLEDGMENTS

TABLE OF CONTENTS

LIST OF TABLES

xvi

LIST OF FIGURES

FIGURES

LIST OF ABBREVIATIONS

AMS	Alpha Magnetic Spectrometer
eV	Electron Volt
GEO	Geostationary and Geosynchronous
HEO	High Earth Orbit
LET	Linear Energy Transfer
LEO	Low Earth Orbit
MBU	Multibit Upset
MEO	Medium Earth Orbit
MeV	Mega Electron Volt
PAF	Proton Accelerator Facility
SAA	South Atlantic Anomaly
SANAEM	Sarayköy Nuclear Research And Training Center
SEB	Single Event Burnout
SEE	Single Event Effect
SEFI	Single Event Functional Interrupt
SEGR	Single Event Gate Rupture
SEL	Single Event Latch-up
SES	Single Event Snapback
SET	Single Event Transient
SEU	Single Event Upset
TAEA	Turkish Atomic Energy Agency
TID	Total Ionizing Dose
TNID	Total Non-Ionizing Dose

CHAPTER 1

INTRODUCTION TO THE IMECE SATELLITE

The dictionary meaning of IMECE in Turkish is " bringing all kinds of different opportunities together ". The IMECE satellite will exemplify this principle by merging current human resources in space studies, heritage gained from past satellites, such as RASAT and Göktürk2, and experimental payloads, towards a national satellite. It will be an Earth observation satellite with the objective of imaging desired regions and enhancing reconnaissance data. Its operation time is planned for 5 years and its orbit will be nearly circular. Several R&D projects have been initialized to build experience in different areas towards the IMECE satellite. While the IMECE satellite project has not yet been officialized, some of its orbit parameters such as the inclination angle, its altitude and its launch date are needed to calculate the space environment in its orbit. To obtain a realistic prediction of the space radiation environment, satellites having similar missions in LEO can be examined.

Generally, Earth observation satellites are located at altitudes above 500 km to avoid the air-drag and below 700 km to have a good visual resolution of the target. For the IMECE satellite, altitude is proposed to as 540 km for the purpose of these studies. In addition, a sun-synchronous orbit where the local solar time is a constant is often suitable as to record comparable data with the same amount of sun light. These orbits are polar and generally have a high inclination angle. Inclination angle for the IMECE satellite calculated for the selected altitude is 98.0 degrees. If the satellite project is initialized just after the submission of this thesis, a satellite like IMECE can be expected to launch in 4 years, which means after 2020. Predicted orbit parameters of the IMECE satellite are presented in Table 1.1. All space environment predictions, simulations and calculations about the IMECE satellite are done with these orbit pa-

rameters that will need to be updated once the project is officially started.

Table1.1: The predicted orbit parameters of IMECE satellite.

Launch date	2020 year
Orbit Type	Low Earth Orbit
Altitude	540 km
Inclination angle	98 degrees
Mission duration	5 years
Eccentricity	0

Material selection and structural design of the IMECE satellite will greatly depend on the characteristics of this space environment. Subsystems of the IMECE satellite are being constructed by TÜBİTAK UZAY in collaboration with different defence and space industry companies and R&D groups at universities in Turkey [1]. A subsystem is a group of components that support a common function. Main subsystems for an ordinary satellite can be grouped as [2]

- Power Subsystem

- Communication Subsystem

- Structure and Mechanisms Subsystem

- Thermal Subsystem

- Platform command and data handling subsystem

- Payload Subsystem

- Attitude and Orbit Control Subsystem

These typical subsystems can be a guide for probable subsystems of the IMECE satellite. A satellite also consists payloads, which are mission-specific and they are often a collection of subsystems [3].

For reliable and robust performance of a satellite in orbit, subsystems are required to be built from modules with flight heritage. If a new technology is being flown to gain the necessary heritage, it is flown as an experimental payload.

Solar cells, Li-Ion battery and multi-layer insulation composite material of the IMECE satellite will be tested as a part of the METU-DBL project. Experimental payloads that are under consideration for flight on the IMECE satellite [4] are:

- Solar panels being developed by TÜBİTAK MAM Materials Institute and Gazi University

- Li-Ion battery being developed by TÜBİTAK MAM Energy Institute

TÜBİTAK UZAY will also develop some payloads of the IMECE satellite [1] that are:

- Electro-optic Satellite Camera

- Star Tracker

- Sun Sensor

- Reaction Wheel

- New Generation Flight Computer

In this thesis, after examining the space radiation environment of the LEO satellites in Section 2.1, the radiation environment of the IMECE satellite by using predicted orbit parameters is simulated and studied using SPENVIS [5] program in Section 2.2. In the following section, literature on radiation effects in matter are given. In Section 2.4, radiation analyses of the solar cell for the IMECE satellite is performed with the GEANT4 [6] program using the space environment output from SPENVIS. In Section 2.5, general characteristics of a radiation environment test are presented. In Chapter 3, simulation results of the defocusing beamline to satisfy the requirements of the ESA-ESCC No:25100 standard [7] are presented. A secondary particle study of the beam hitting the foils and collimators, radiation dose around the beamline and protection of the target area from secondary particles are analysed in detail. In Chapter 4, a preliminary study to perform radiation environment tests for materials intended for nuclear reactors is given. The conclusion is provided in Chapter 5.

CHAPTER 2

RADIATION ENVIRONMENT PREDICTIONS FOR THE IMECE SATELLITE

2.1   Space Radiation Environment in LEO

There are three altitude classifications for satellite orbits: Low Earth Orbit (LEO), Medium Earth Orbit (MEO) and Geosynchronous Orbit (GEO). Their altitude ranges can be seen in Table 2.1. Different altitude ranges result in different types of space radiation to dominate in an orbit's environment. Space radiation in Earth orbit can be categorized as resulting from Galactic Cosmic Radiation (GCR), Solar Particle Events (SPE) and Trapped Radiation, which will be now be presented [8].

Table2.1: Satellite altitude ranges of different Earth orbit types [9].

Orbit Type	Altitude Range
Low Earth Orbit (LEO)	160 km - 2,000 km
Medium Earth Orbit (MEO)	2,000 km - 35,786 km
Geosynchronous Orbit (GEO)	About 35,786 km

Galactic cosmic radiation consists of primary particles, accelerated at astrophysical sources, which come from outside the solar system. Cosmic radiation propagating through the interplanetary medium or the atmosphere undergoes nuclear collisions and generates secondary cosmic rays [10]. The primary cosmic rays observed in Earth orbit comprise about 85 % protons, 14 % helium nuclei and 1 % heavier nuclei with energies up to 1 GeV [11]. Particles and nuclei produced in stellar nuclear reactions are considered primaries while elements such as boron and beryllium can

only be produced in collisions of cosmic rays and therefore they are considered as secondaries. Generally, components of primary cosmic rays show a flux distribution that decreases with a 2.7 power law of increasing kinetic energy. The AMS-02 (Alpha Magnetic Spectrometer), a high energy physics experiment on the International Space Station [12], observed this behavior for protons, as seen in Figure2.1. A precision measurement of the proton flux in primary cosmic rays with rigidities (defined as momentum per charge) franging from 1 GV to 1.8 TV is presented. The flux multiplied by $E_K^{2.7}$ deviates from a single power law and progressively hardens at high rigidities [13]. At lower energies, the spectrum is modulated by the solar wind, which is the expanding magnetized plasma generated by the Sun [14].
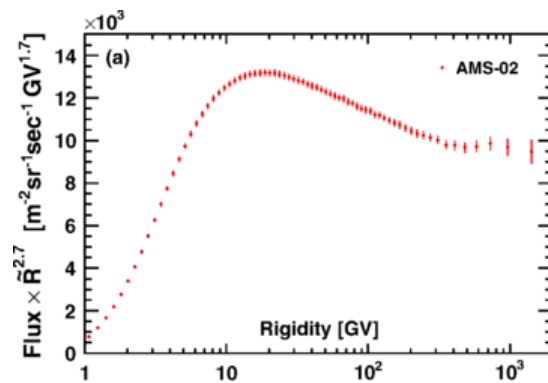
Figure 2.1: The AMS-02 proton flux multiplied by $R^{2.7}$ as a function of rigidity. The flux multiplied by $E_K^{2.7}$ deviates from a single power law and progressively hardens at high rigidities. [13].

Solar particle events caused by solar energetic particles occur when the Sun releases a huge amount of energy in the solar atmosphere. The energy of these particles range from keVs to GeVs. Most large and complex solar energetic particle events are accelerated by Coronal Mass Ejections (CME) related to shocks in the corona and in the interplanetary space near the Sun. In contrast, impulsive solar particle events are accelerated by solar flares with a huge magnetic energy released on the Sun's surface [10, 15].

The shape of the magnetosphere of the Earth allows for regions where charged particles can be trapped. Earth's magnetic field concentrates large fluxes of ionizing particles that include protons, electrons, and heavy ions in regions, called Van Allen Belts [12]. These belts are composed of two regions; an inner radiation belt and an

outer radiation belt, shown in Figure 2.2 [8]. The inner belt contains a population of protons with kinetic energies more than 10 MeV while the outer belt contains mainly electrons with energies up to 10 MeV. Trapped particles move in a combination of three periodic motions; circular motion around the Earth's field lines, oscillating motion along field lines between two mirror points and longitudinal drift around the Earth as seen in Figure 2.3. Electrons drift towards the East while protons drift West [16].
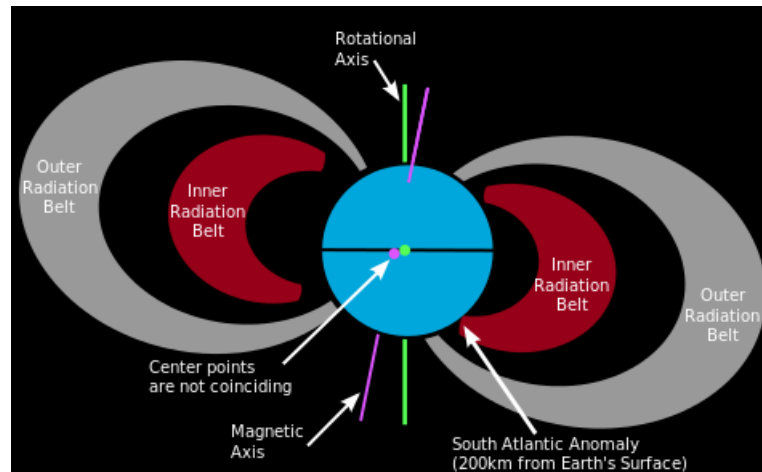
Figure 2.2: There is approximately 11 degrees between the rotational axis and magnetic axis of the Earth and intersection point of these axes is not located at the Earth's center. Due to this asymmetry, a region called the South Atlantic Anomaly (SAA) is exposed to a higher flux of trapped particles than other regions. These trapped particles concentrate on two radiation belts named as the Inner and the Outer radiation belts around the Earth [17].

Low altitude trapped proton and electron fluxes depend on the variation of solar irradiance during the solar cycle. The Sun has an 11-year cycle at the end of which the magnetic field flips [19]. The number of sunspots start at a maximum, called the solar maximum, then reach a minimum after around 5.5 years and then reach the maximum again when a new solar cycle starts. Figure 2.4 shows the number of sunspots during the last 130 years, which correlates well with the Sun's activity. During the solar maximum, Earth's neutral atmosphere expands compared to the solar minimum, which causes the low altitude edges of the radiation belts to be destroyed due to increased interactions with neutral constituents [20]. Thus, the maximum flux
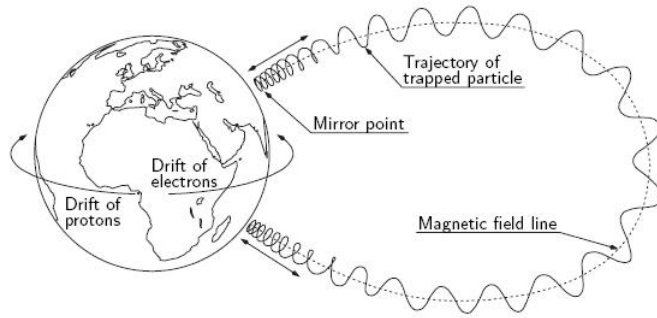
Figure 2.3: Basic motions of trapped particles, in the Earth's magnetic field, are circular motion around the Earth's field lines, oscillation along field lines around the plane between two mirror points and longitudinal drift around the Earth [16].
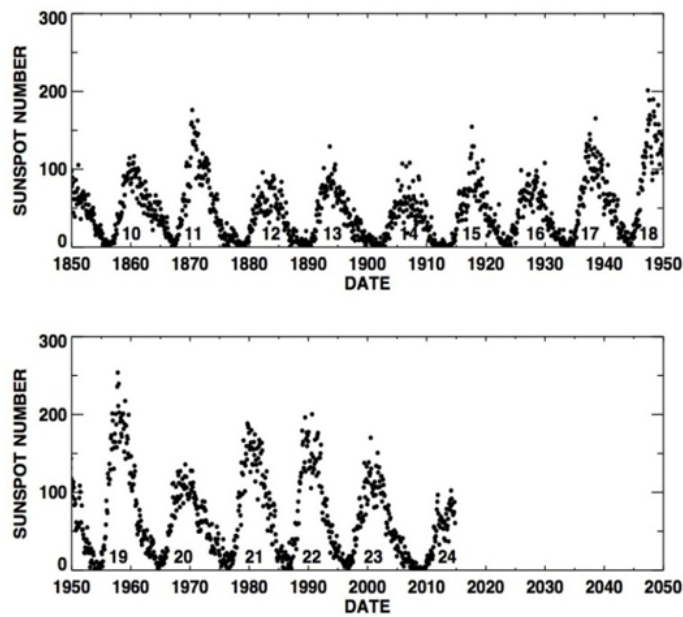
Figure 2.4: The number of sunspots during the last 130 years correlates well with the Sun's activity. The 11 year long solar cycle period includes a solar maximum and a minimum [18]. The current 24th cycle, counted from 1750 when first records began, reached its maximum in 2014.

of trapped protons appears at the solar minimum. In contrast, when the solar flux reaches its maximum, the flux of trapped electrons reaches its maximum.

The Van Allen radiation belts are symmetrical around the Earth's magnetic axis, which is tilted with respect to the Earth's rotational axis by an angle of approximately 11 degrees. In addition, the intersection between the magnetic and rotational axes of the Earth is not located at the Earth's center. Because of this asymmetry, the inner Van Allen belt is closest to the Earth's surface over the South Atlantic Ocean [21, 22]. This causes an anomalous increased flux of energetic particles in this region, called the South Atlantic Anomaly (SAA). Therefore, satellites and other spacecraft passing through the SAA require appropriate shielding and precautionary measures such as shutting down critical components or frequent resets. Otherwise, they can lose critical subsystems which lead to shortened service. For example, the guidance system of the Hubble Space Telescope HST (STS-31) located at an altitude of 547 km was affected on the 5th of May in 1990 during a solar maximum when the telescope was passing through the South Atlantic Anomaly (SAA). Bit flips occurred in the RAM of the Fine Guidance Electronics. On the 6th of December in the same year, another passage through the SAA caused high photomultiplier tube (PMT) counts in the fine guidance system. This resulted in guide star acquisition failures. Both incidents were suspected to be due to the increased radiation levels in the solar maximum [23].

To develop an insight on the space radiation environment of a satellite, an understanding of dominating particle fluxes in its orbit is necessary. For the IMECE satellite, electrons and protons trapped in the Earth's magnetic fields are the leading source of radiation in its orbit. Space radiation environment predictions from SPENVIS for the IMECE satellite now will be presented in detail in the next section.

2.2 Space Environment Predictions for the IMECE Satellite

To predict and model the space environment of the IMECE satellite, SPENVIS (The Space Environment Information System) is employed. In SPENVIS, a spacecraft's trajectory or coordinate grid can be defined so that radiation sources and effects can be analysed for the defined orbit. The orbital parameters for the IMECE satellite, given in Table 1.1, are defined in SPENVIS. The resulting trajectory of IMECE during its

mission time can be seen Figure 2.5 in 2-D and in 3-D. The color scale shows the altitude of the IMECE satellite. Although the orbital radius of IMECE is defined as a constant, the altitude varies along its trajectory due to the oblate nature of the Earth [24]. As a result, the altitude of the IMECE satellite reaches its minimum around the Equator while it reaches its maximum around the poles.
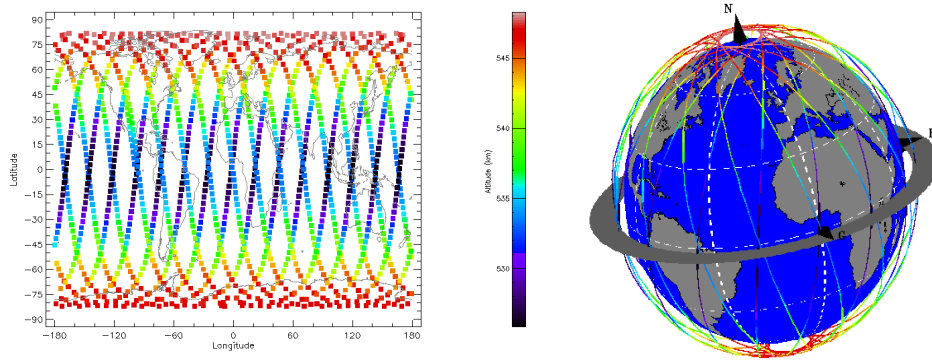
Figure 2.5: 2-D and 3-D trajectory simulations of the IMECE satellite as calculated from SPENVIS. The color scale shows the altitude of the IMECE satellite. Although the orbital radius of the IMECE satellite is defined as a constant, the altitude varies due to the oblate nature of the Earth. As a result, the altitude of the IMECE satellite reaches its minimum around the Equator while it reaches its maximum around the poles.

SPENVIS can calculate the flux of primary and trapped particles during IMECE's mission time in a given orbit. For the IMECE satellite, LEO space environment is considered; therefore, low-energy trapped particle flux dominates. NASA's AE8-MAX model contains the worst case for trapped electrons and AP-MIN model, the worst case for trapped protons, mentioned in Section 2.1 [19]. These models, based on data from more than 20 satellites from the early 60's to the mid-70's, are selected as input in SPENVIS [19]. By using these models, SPENVIS gives the integrated number of trapped particles over a certain energy, per unit area per second, called the integral flux. Figure 2.6 shows the integral flux of trapped electrons with kinetic energies higher than 0.04 MeV while Figure 2.7 gives the integral flux of trapped protons with kinetic energies higher than 0.15 MeV with respect to the coordinates of the IMECE satellite. Color scales show the integral fluxes of trapped electrons and
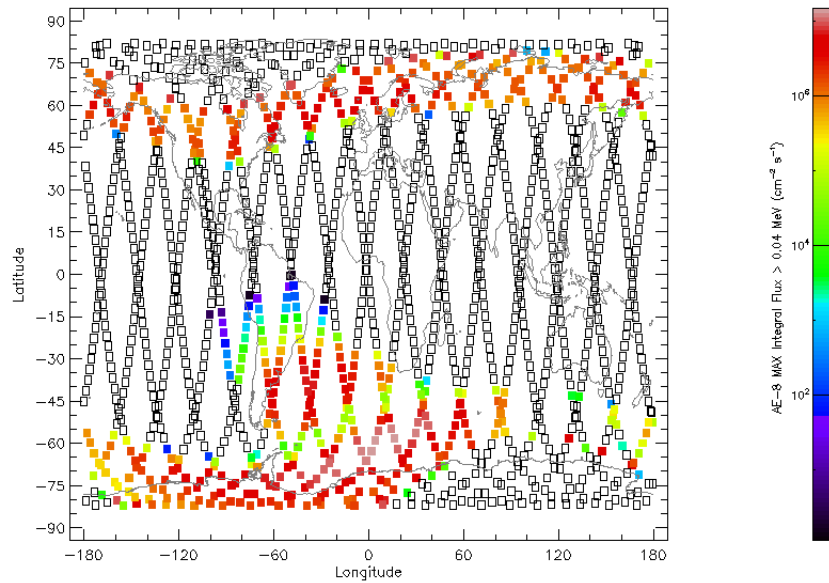
Figure 2.6: The integral flux of trapped electrons with respect to the coordinates of the IMECE satellite as calculated from SPENVIS. The color scale shows the integral flux of trapped electrons with kinetic energies higher than 0.04 MeV during the solar maximum. A high flux region over the SAA and poles are clearly visible.

protons. In Figure 2.6, the high flux of trapped electrons occurs in the poles and the SAA. The high flux of the trapped protons can be clearly seen in the SAA in Figure 2.7.

SPENVIS also gives the particle flux density per unit energy incident on a unit area per second, called the differential flux. The worst case with highest foreseen differential flux with respect to the kinetic energy of trapped particles can be seen respectively for electrons in Figure 2.8 and for protons in Figure 2.9. The electron flux dominates over the proton flux by three orders of magnitude below 1 MeV. According to the results of the AMS-01 experiment which flew on the shuttle, Endeavour in 1998 at an altitude of 380 km, the trapped particle spectrum heavily depends on the geomagnetic latitude of the satellite. Primary protons that impinge on the equatorial plane of the geomagnetic environment are deflected towards the poles due to the Lorentz's magnetic force, if proton's energy is less than 10 GeV. Only particles above a certain kinetic energy, called the geomagnetic cutoff rigidity, defined in Equation 2.1, can

11
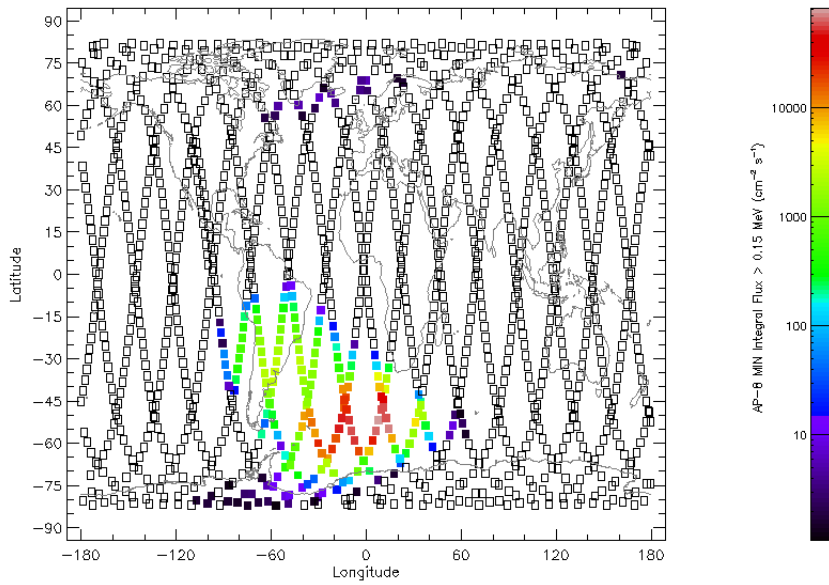
Figure 2.7: The integral flux of trapped protons with respect to the coordinate of the IMECE satellite as calculated from SPENVIS. The color scale shows the integral flux of trapped protons with kinetic energies higher than 0.15 MeV during the solar minimum. A high flux region over the SAA is clearly visible.
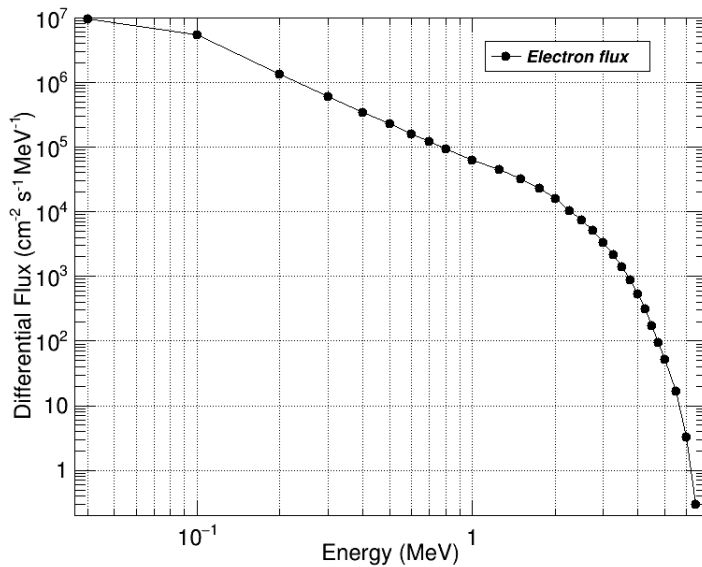
Figure 2.8: Energy vs differential flux for trapped electrons for the IMECE satellite's path for its mission time as calculated from SPENVIS.
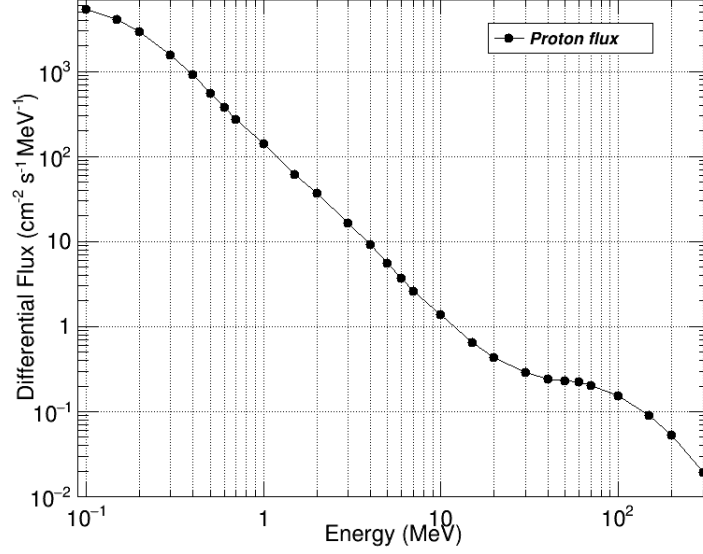
Figure 2.9: Energy vs Differential Flux for trapped protons for the IMECE satellite's path for its mission time as calculated from SPENVIS.

enter as they are minimally deflected.

$$R_c = \frac{M\cos^4\lambda}{R^2(\sqrt{1 + \cos\alpha\cos^3\lambda} + 1)^2} \tag{2.1}$$

In this formula, R_c represents the cutoff rigidity in GV and M is normalized magnetic dipole moment of the Earth. In addition, α is the angle of arrival of a positive ion, R is geocentric radius in km and λ is the magnetic latitude. At the poles, the magnetic field lines and the momentum of the particle is nearly collinear. Therefore, the magnetic force is close to zero and particles of any energy can enter the Earth's geomagnetic environment and subsequently be trapped in it [12]. The differential spectra in terms of kinetic energy for downward and upward going protons, collected within 32° of the AMS-01 z-axis, are presented in Figure 2.10. Downward going particles through AMS-01 are shown on the top panels (a,b,c) while upward going particles are shown in the lower panels (d,e,f). The results have also been separated according to the absolute value of the corrected geomagnetic latitude, θ_M (radians), where they were detected by AMS-01. Figure 2.10 a, b and c clearly show the effect of the geomagnetic cutoff and the decrease in this cutoff with increasing θ_M. The spectra above and below the cutoff differ. The spectrum above the cutoff is referred to as the "primary particle" spectrum and below cutoff as the "trapped particle" spectrum

13

[12]. In Figure 2.10, the observed spectrum of upward going particles matches the lower energy spectrum of the downward particles in (a,b,c), which proves that these particles are indeed trapped in the Earth's geomagnetic environment.
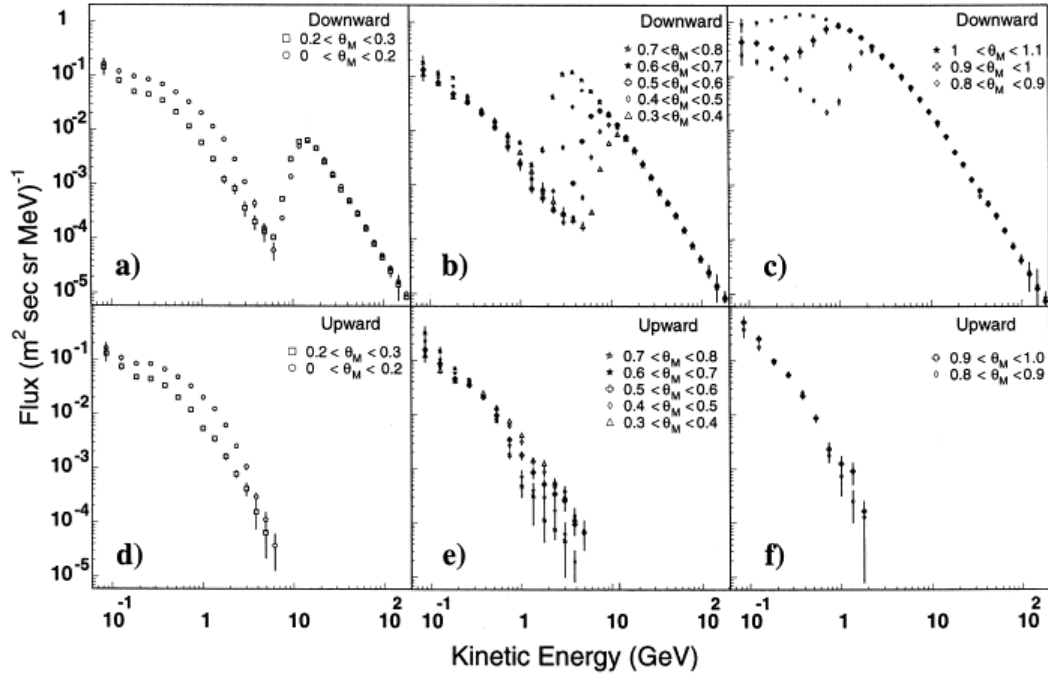
Figure 2.10: AMS-01 flux spectra (a,b,c) for downward and (d,e,f) for upward going protons according to the geomagnetic latitude,θ_M,where they were detected [12]. The a, b and c clearly show the effect of the geomagnetic cutoff and the decrease in this cutoff with increasing θ_M. The spectra above and below the cutoff differ. The spectrum above the cutoff is refered to as the "primary particle" spectrum and below cutoff as the "trapped particle" spectrum [12]. The observed spectrum of upward going particles matches the lower energy spectrum of the downward particles in (a,b,c), which proves that these particles are indeed trapped in the Earth's geomagnetic environment.

It should be noted that the highest geomagnetic cutoff of 10 GV for the IMECE satellite occurs at the Equator ($\lambda=0$) and for a perpendicular coming particle ($\alpha=0$). Except at the poles, the trapped spectrum dominates over the primary spectrum for IMECE.

14

2.3 Radiation Effects in Matter

Satellites and other spacecraft need to be tolerant to space radiation until the end of their mission time. To understand how this radiation environment affects them, interaction of particles with matter must be studied first.

Radiation can be classified as ionizing and non-ionizing radiation. Ionizing radiation deposits energy into the material with which it interacts, by ionizing or exciting the electrons. Non-ionizing radiation is generally caused by neutral particles interacting with the nuclei in the material.

Two principle features characterize the passage of charged particles through matter. One of them is a loss of energy of the particles caused by collisions with the electrons in the material. The another principle is a deflection of the particle from its incident direction caused by hard scattering from nuclei [25]. Inelastic collisions are responsible for the energy loss of heavy particles such as protons and alpha particles in matter. Generally, the amount of energy transferred during collisions is a very small fraction of the particle's kinetic energy and the fluctuations at each step of the total energy loss are very small. Therefore, the average energy loss per unit path length is a more meaningful quantity, often called the *stopping power* or dE/dx. This quantity was first calculated by N. Bohr and later developed by H. Bethe, F. Bloch and others. They calculated energy transfer in terms of momentum transfer because it is measurable quantity. The obtained formula can be seen in Equation 2.2. The Bethe-Bloch formula also contains the Shell (C) and Density (δ) corrections that are important at high and low energies respectively.

$$-\frac{dE}{dx} = 2\pi N_a r_e^2 m_e c^2 \rho \frac{Z}{A} \frac{z^2}{\beta^2} \left[\ln \left(\frac{2m_e \gamma^2 \nu^2 W_{max}}{I^2} \right) - 2\beta^2 - \delta - 2\frac{C}{Z} \right] \qquad (2.2)$$

In the above equation, some important quantities are:

$2\pi N_a r_e^2 m_e c^2 = 0.1535 MeV c^2/g$

r_e: classical electron radius

m_e: electron mass

ρ: density of absorbing material

Z: atomic number of absorbing material

15

z: charge of incident particle in units of e

A: atomic weight of absorbing material

W_{max}: maximum energy transfer in a single collision

It is very important that energy loss depends on the square of the charge of the incident particle and the density of absorbing material. For example, an alpha particle travels only a few centimeters in air, but an alpha particle with 5 MeV kinetic energy stops at 23 μm in silicon [26]. Another example is that the energy loss by a proton with 30 MeV kinetic energy is four times smaller than the energy loss by a helium nucleus with the same energy. That is, a helium nucleus can do more damage to a material or component that it passes through due to this energy transfer. If this energy loss process occurs continuously in a material or component, the cumulative effect can be described as Total Ionising Dose (TID). The deposition of energy in a material by means of ionization is conventionally termed " dose " and measured in rad or $Gray$ [11]. 1 $Gray$, an amount of absorbed energy per kilogram of matter, is equal 100 rad. The cumulative long term ionizing damage, often due to protons and electrons in space, can cause threshold shifts, increased power consumption, timing changes and decreased functionality of devices. The effect of electrons and low energy protons can partially be reduced with a few millimeters of shielding material around sensitive devices.

While cumulative effects can occur as a result of long exposure to radiation, transient or destructive effects due to single particles, often called Single Event Effects (SEEs), can also occur in devices and components in the space radiation environment. SEEs arise through the action of a single ionizing particle as it penetrates sensitive components of electronic devices. Single events can lead to randomly appearing problems and errors that may cause system failures in electronic systems. There are a variety of single events effects, listed in Table 2.2 [27]. Some SEEs are destructive such as SEL, SEB, SEGR while others are nondestructive such as SEU, SET, SES and MBU. Nondestructive SEEs can be corrected if caught in software or be recovered from using a soft-reset [28].

SEE is often parameterized with respect to the stopping power called linear energy transfer (LET). LET is the energy deposited per unit path length given in Equation 2.3 where ρ is the density of the target material and the LET has a unit of MeV/mg/cm^2

Table2.2: Basic types of Single Event Effects (SEEs) and errors caused by their effects.

SEU	Upset	Temporary change of memory or control bit
SET	Transient	Transient introduced by single event
SEL	Latchup	Device latches in high current state
SES	Snapback	Regenerative current mode in NMOS
SEB	Burnout	Device draws high current and burns out
SEGR	Gate Rupture	Gate destroyed in power MOSFETS
SEFI	Functional Interrupt	Control path corrupted by an upset
MBU	Multibit Upset	Several bits upset by the same event

[27]. Another important quantity related to SEEs is the cross section σ, which is the device SEE response to ionizing radiation. In an experimental test for a specific LET, the SEE cross section gives the number of errors per ion or proton fluence. The unit generally used for the SEE cross section is cm^2 per device or per bit [29]. SEEs occur when the collected fraction of the charge liberated by the ionizing particle is larger than the electric charge stored on a sensitive node [30].

$$LET = -\frac{1}{\rho}\frac{dE}{dx'} \qquad (2.3)$$

If the LET of the charged particle is greater than the amount of energy or critical charge required, an effect may be seen as soft errors such as upsets (SEUs) or transients (SETs), or hard (destructive) errors such as latchup (SEL), burnout (SEB), or gate rupture (SEGR) [31].

SEEs can be caused by heavy ions or protons passing through electronic devices. There are two primary damage mechanisms of ionization: direct and indirect. Direct ionization is often a result of a heavy ion, passing through the material and depositing a large amount of energy in the sensitive volume. The indirect one is caused by a proton as can be seen in Figure 2.11 that hard scatters a heavy nucleus near the sensitive device area, which then deposits a large amount energy into this volume [32].

Hadrons such as protons and heavy ions can also cause Displacement Damage (DD) effects on photonic or optoelectronic devices such as Lasers, LEDs, Optical receivers and Opto-couplers [33]. An incident hadron will create defects by colliding with an atom in the crystal lattice, which causes significant change to the electrical charac-
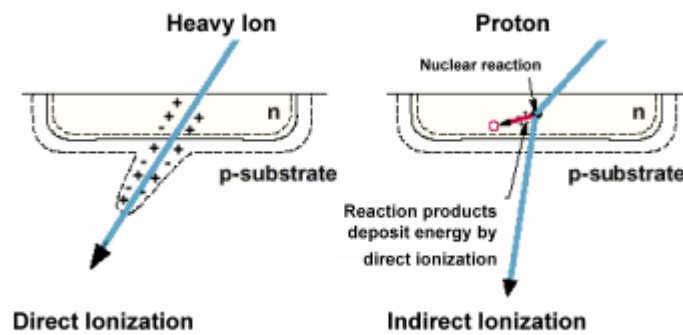
Figure 2.11: Ionization paths from direct ionization (heavy ions) and from indirect ionization (protons) in a semiconductor device [32].

teristics of certain components. Displacement Damage can also be caused by non-ionizing radiation.

Non-ionizing radiation refers to an often low-energy but still harmful radiation in which particles transmit energy into the material with which it interacts, but does not directly remove electrons. Most non-ionizing radiation that is received in space flight is often secondary radiation. When a charged particle interacts with the shielding material of the satellite, neutral particles such as short-lived pions and neutrons are produced. The cumulative long term non-ionizing radiation is often called Total Non-ionizing Dose to differentiate the kind of DD from those caused by ionizing radiation.

Another phenomenon related to radiation is Bremsstrahlung, called Braking Radiation. It applies to particles with an electrical charge, whose velocity is close to the speed of light. It occurs when a relativistic particle interacts with a strong electric or magnetic field. In contrast to protons, the relative small mass of electrons causes them to be easily deflected by collisions with atomic electrons and nuclei. This in turn causes them to produce bremsstrahlung, which is much more penetrating than electrons. Thus, radiation protection from bremsstrahlung can be an important consideration for satellites in space [34].

Satellites and other spacecraft can be exposed to the radiation effects, detailed above, in their orbits or during and after launch. Radiation-hardness is defined as ensuring

reliable operation of electronics with no loss of performance while working in an environment with radiation [35]. Radiation-hardness is often a requirement of GEO and beyond Earth-orbit missions. Components that can withstand such high doses are necessarily very expensive due to the long R&D, testing and qualification procedure. However, testing components to the doses that it will receive with some safety factor results in the development of radiation-tolerant devices, which allows reliable satellites to be designed at a reasonable cost. Underestimating the radiation environment leads to an excessive risk for the satellite. This can result in degraded performance and a shortened mission lifetime. On the other hand, overestimating the radiation environment can result in over-design by engineers. This can increase the cost of the satellite and even limit some of its capabilities [36].

2.4 Radiation Dose Predictions for the IMECE Satellite and Solar Panels

Most electrical and sensitive components located inside the volume of the satellite are often shielded by a few millimeters of aluminium, which stop most of the low energy trapped electrons and some of the low-energy protons impinging on the satellite. To ensure reliable performance of components used in satellites, dose prediction and tests of said components to that dose are critical before launching them. Absorbed dose for a simplistic satellite can be predicted in the SPENVIS program and plotted as a function of the thickness of some shielding. The program takes an aluminium sphere which is under 4π uniform radiation and gives the dose deposited in this sphere. A GaAs sample is located in this volume to allow for a comparison of the IMECE solar cell radiation analysis as thickness of the shielding goes to zero. Such a plot for the IMECE satellite can be seen in Figure 2.12. According to this graph, the electron flux decreases with increasing thickness of aluminium, while the trapped proton flux remains nearly constant after a sharp drop around 2 mm shielding thickness. For this reason, a few millimeters thick aluminium is often used for shielding satellites for optimum radiation dose, cost and weight balance.

While some components are located inside this safer shielded volume, some modules such as solar panels and antennas are necessarily located outside this volume and they are exposed to the full spectrum of trapped particles and cosmic rays, in-
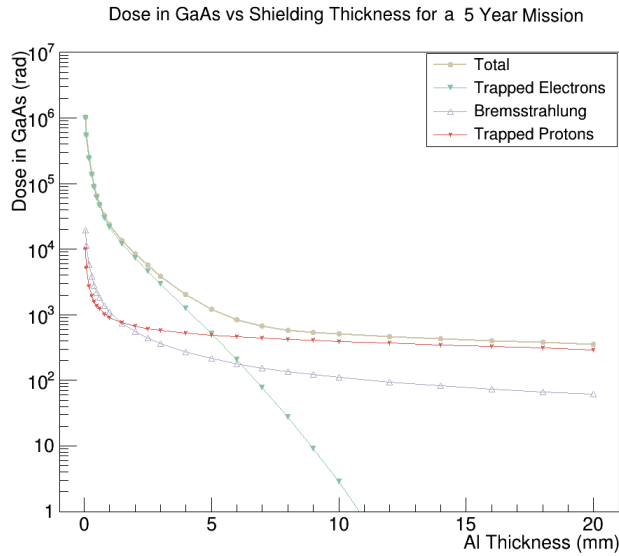
Figure 2.12: Absorbed dose for a GaAs sample can be predicted in the SPENVIS program and plotted as a function of the thickness of aluminium shielding for different particles in the space radiation environment of the IMECE satellite.

cluding electrons, protons and heavy ions. These particles can damage the structure of components and affect their operation negatively [37]. For this reason, the solar cell structure planned for the IMECE satellite, was analysed layer by layer in order to understand the radiation effects of trapped charged particles in its space environment. The preliminary structure of the solar cell in production by Gazi University is shown in Figure 2.13 [38]. The area of the solar cell is 3 cm × 6 cm. Except Germanium layers, all other layers are p-doped with Silicon and n-doped with Beryllium. The bottom-most Germanium layer is doped with Gallium and the one above is doped with Arsenic. Contact (silver or gold) and doping concentration of Cerium in protective glass and the thicknesses of Al_2O_3 and TiO_2 layers have not yet been finalized in the design. For the purpose of this simulation, both the Al_2O_3 and TiO_2 layers are taken to be 50 nm thick and glass is doped with 1% Cerium [38].

Reliable and efficient operation of the solar panels is critical to the successful completion of IMECE's mission. Therefore, radiation absorption and secondary particle production in solar cell layers are simulated with GEANT4 in the space radiation environment obtained from SPENVIS shown in Figure 2.8 for electrons and Figure 2.9 for protons. Visual output of the protons striking the solar cell structure of the

20

Layer	Thickness (nm)	Carrier Concentr. (cm^{-3})
n^{++} GaAs	250	5,0x10^{18}
n^{+} AlInP	25	1,0x10^{19}
n-In$_{0,49}$Ga$_{0,51}$P	200	1,8x10^{18}
p- In$_{0,49}$Ga$_{0,51}$P	750	1,0x10^{18}
p+AlInGaP	25	1,0x10^{19}
p^{++} GaAs	20	3,0x10^{19}
n^{++} GaAs	20	5,0x10^{19}
n+InGaP	20	1,0x10^{19}
n-GaAs	200	2,0x10^{18}
p-GaAs	350	2,0x10^{16}
p+InGaP	20	1,0x10^{19}
p^{++} GaAs	20	3,0x10^{19}
n^{++} GaAs	20	5,0x10^{19}
n^{+}AlGaAs	25	1,0x10^{19}
n-Ge	150	2,0x10^{17}
p-Ge	1.5x10^{5}	2,0x10^{17}
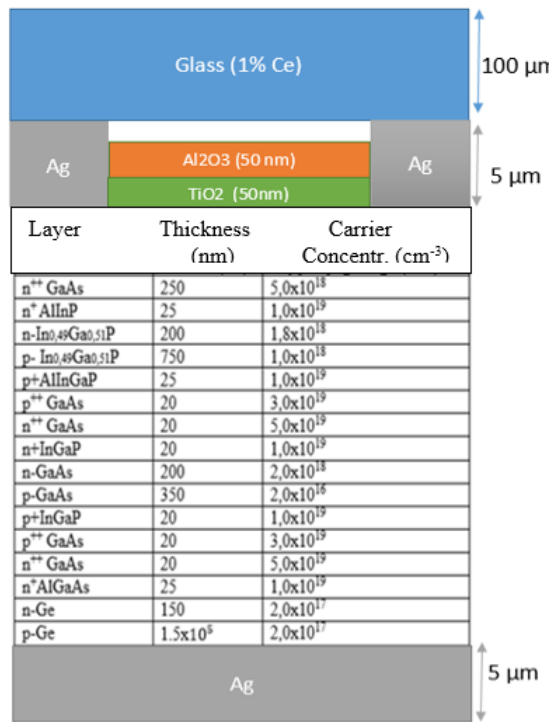
Figure 2.13: Except Germanium layers, all other layers are p-doped with Silicon and n-doped with Beryllium. The bottom-most Germanium layer is doped with Gallium and the one above is doped with Arsenic. Contact (silver or gold) and doping concentration of Cerium in protective glass and the thicknesses of Al_2O_3 and TiO_2 layers have not yet been finalized in the design. Both the Al_2O_3 and TiO_2 layers are taken to be 50 nm thick and glass is doped with 1% Cerium for preliminary solar cell structure of the IMECE satellite.

IMECE satellite is shown in Figure 2.14 [39]. In this simulation, blue lines show the path of incoming protons, which are generated at yellow points on the surface of a sphere. The rectangle is the solar cell structure and also the coordinate system of the solar cell structure can also be seen as red, blue and green arrows.

Full spectrum of trapped particles during 5 years of IMECE operation are simulated impinging the solar cell randomly and the resulting secondary particles. Their mean kinetic energy and flux can be seen in Table 2.3 for trapped electrons and Table 2.4 for trapped protons. Gammas and electrons produced by trapped electrons have kinetic energies less than one hundred keV and a high flux. In contrast, gammas, secondary protons, electrons, neutrons and alphas produced by trapped protons have kinetic energies between 1-10 MeV but a low flux. In addition, Total Ionising Dose (TID) in the solar cell and effects of secondary particles on TID were analysed in detail. According to Table 2.5, almost all TID on the solar cell originates from trapped electrons due to their unshielded high flux. Therefore, solar cell should be tested with an electron beam with a few MeV kinetic energy before qualifying for flight.
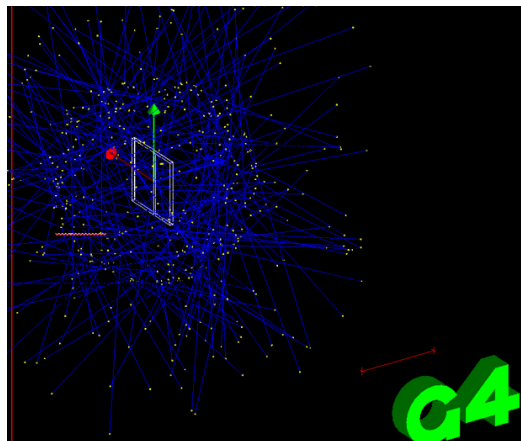
Figure 2.14: Blue lines show the path of protons, which are generated at yellow points on the surface of a sphere. The rectangle is the solar cell structure and also the coordinate system of the solar cell structure can be also seen as red, blue and green arrows.

Critical fluence damage coefficients can be employed to construct a model in which the various components of a combined radiation environment can be described in terms of a damage equivalent fluence produced by energetic particles of a single energy [40, 41]. For this reason, 1 MeV electron fluence has been used as a basis for the

Table2.3: The flux and mean kinetic energy of gamma and electron production in the solar cell from the trapped electron radiation for one second in orbit.

Secondary particles	Mean kinetic energy	Flux (p/cm^2/s)
Gamma	84.9 keV	6.78×10^3
Electron	49.2 keV	2.93×10^3

Table2.4: The flux and mean kinetic energy of gamma, proton, electron, neutron and alpha production in the solar cell from the trapped proton radiation for one second in orbit.

Secondary particles	Mean kinetic energy	Flux (p/cm^2/s)
Gamma	1.64 MeV	1.13×10^{-1}
Proton	13.7 MeV	4.86×10^{-2}
Electron	0.38 MeV	3.11×10^{-2}
Neutron	8.61 MeV	6.05×10^{-2}
Alpha	7.44 MeV	1.50×10^{-1}

Table2.5: TID coming from trapped protons and electrons and effects of secondary particles on total dose during 5 years of operation time of the IMECE satellite.

Particle Type	Trapped Protons	Trapped Electrons
Total Ionising Dose	10.3 krad	1700 krad
Effect of secondary particles on dose	0.16%	0.18%

damage equivalent fluence which emulate the total solar cell degradation. Similarly, proton damage can be normalized to the damage produced by protons of a specific energy. The proton energy employed for normalization of relative damage should be an energy that occurs in the space environment, that produces relatively uniform damage, and is commonly available in accelerator laboratories. The difficulty with the low energy protons in establishing damage equivalence arises from the fact that the range of protons with energies below 1 MeV in GaAs is less than the active solar cell thickness. While 1 MeV energy protons produce non-uniform damage, 10 MeV protons fulfill these requirements and are therefore commonly used as a basis for calculating and testing equivalent proton damage in solar cells [42].

As a part of METU-DBL project, the solar cell of the IMECE satellite will be tested with 10 MeV kinetic energy protons. The minimum proton energy given by the accelerator used by the METU-DBL project is 15 MeV. To test solar cells of the IMECE satellite, this energy must be decreased to 10 MeV by using some beam elements. Studies to satisfy this requirement will be shown in Chapter 3. Testing with an electron beam with 1 MeV kinetic energy is also essential to ensure the radiation tolerance of a solar cell. An accelerator laboratory satisfying this requirement has not yet been found in Turkey, but laboratory visits are underway.

All components used in a satellite may not be tested with the full spectrum of particles in its orbit. For this reason, some simulation programs are developed for space radiation and radiation shielding analysis. The one of them is FASTRAD 3D Radiation Software [43] for used for advanced radiation dose analysis and shielding optimization. It works with a previously defined CAD file of all components of a satellite and can analyze the sensitive parts and local shielding of these parts. During the FASTRAD training in Toulouse in June 2016, a satellite defined in a CAD file is analysed in detail and its input can be seen in Figure 2.15 [44]. This satellite was be exposed to a radiation environment its defined orbit and its sensitive parts were analysed. Also, some sector shielding studies were done for these sensitive parts.
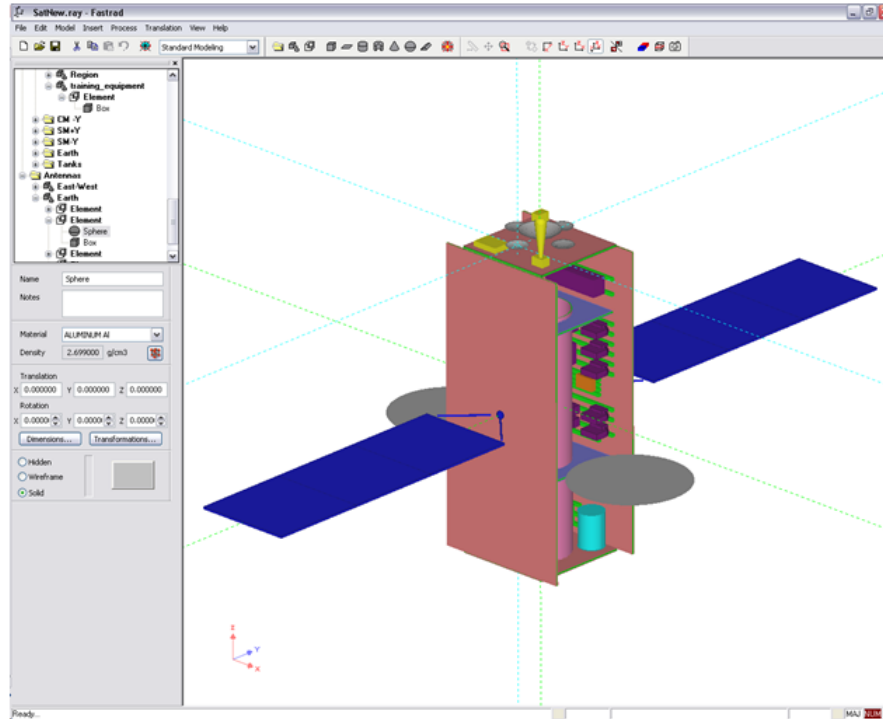
Figure 2.15: Defining a satellite with a CAD file in FASTRAD [44].

2.5 Space Radiation Environment Tests

Energetic particles or photons passing through electronic components and materials used in satellites lose their kinetic energy through a variety of interactions causing damage detailed in Section 2.3 [11]. Thus, these components must be tested and their radiation-tolerance must be analysed before launching the satellites. Three typical tests exist and they are classified as Displacement Damage tests, Single Event Effects (SEE) tests and Total Ionizing Dose (TID) tests.

Currently, TID tests can be performed but SEE tests and DD tests can not be performed in Turkey. Gamma Irradiation Facility at the Turkish Atomic Energy Agency (TAEA) Sarayköy Nuclear Research and Training Center (SANAEM) can be employed for TID tests. This facility has a ^{60}Co gamma source with an activity level of about 250 kCi [45], which is the primary source to implement TID tests. For example, TID tests of GaAs-based Solid State Power Amplifiers (SSPA) components are performed in this facility following the ESA/SCC Basic Specification No.22900 standard [46]. Acceptable dose rates, irradiation steps and periodic measurements for

these tests are defined in these TID standards. Commonly followed standards for TID tests can be seen in Table 2.6.

Table2.6: Some of TID test standards and test methods.

ESCC 22900	Total Dose Steady-State Irradiation Test Method
MIL-STD883G	Ionizing Radiation (Total Dose) Test Procedure
MIL-STD750E	Steady-state Total Dose Irradiation Procedure

While performing TID tests, the dose rate is a critical parameter: the amount of degradation at a given total dose is greater if administered at a Low Dose Rate (LDR) rather than at a High Dose Rate (HDR). This effect is tested with the Enhanced Low Dose Rate Sensitivity especially for sensitive and critical components [28]. Currently, this test can be performed in Turkey by using the ^{60}Co gamma source in NUBA (Nuclear Science Application and Research Center) in Akdeniz University [47].

SEE tests and DD tests can not yet be carried out in Turkey. While this thesis outlines an effort to perform SEE tests at low energies, some facilities can perform both SEE and DD tests with protons and heavy ions. Examples of some facilities, providing beams of different particles, energy ranges and currents in the World are shown in Table 2.7.

Table2.7: Some facilities which can perform SEE tests with protons, their maximum kinetic energies and highest flux.

Place	Facility name	Max KE	Max Flux
PSI[48]	Proton Irradiation Facility	230 MeV	2×10^9 p/cm^2/s
CERN[49]	Irradiation Facility	24 GeV	8.3×10^9 p/cm^2/s
UCDAVIS[50]	Crocker Nuclear Lab	67.5 MeV	1.6×10^{10} p/cm^2/s
UCL[51]	Cyclotron Resource Centre	62 MeV	2×10^8 p/cm^2/s

In Turkey, a Proton Accelerator Facility (PAF) was inaugurated in the TAEA SANAEM center on the 12th May, 2012. A 2-D drawing of this facility can be seen in Figure 2.8 [52]. At center of the facility, a cyclotron is located that can accelerate protons up to a kinetic energy ranging from 15 MeV to 30 MeV. Four irradiation rooms are available in the facility for different purposes. Three of them are used for production

of radioisotopes and later to be chemically converted into radiopharmaceuticals. A fourth and larger room is reserved for R&D experiments. The size of this room is 10.8 m × 8.6 m. There is also an accelerator technical room, containing cooling systems necessary for the facility. Cooling system of METU-DBL will be also located at this room and cooling water will be provided by already existing pipes between the technical room and the R&D room.
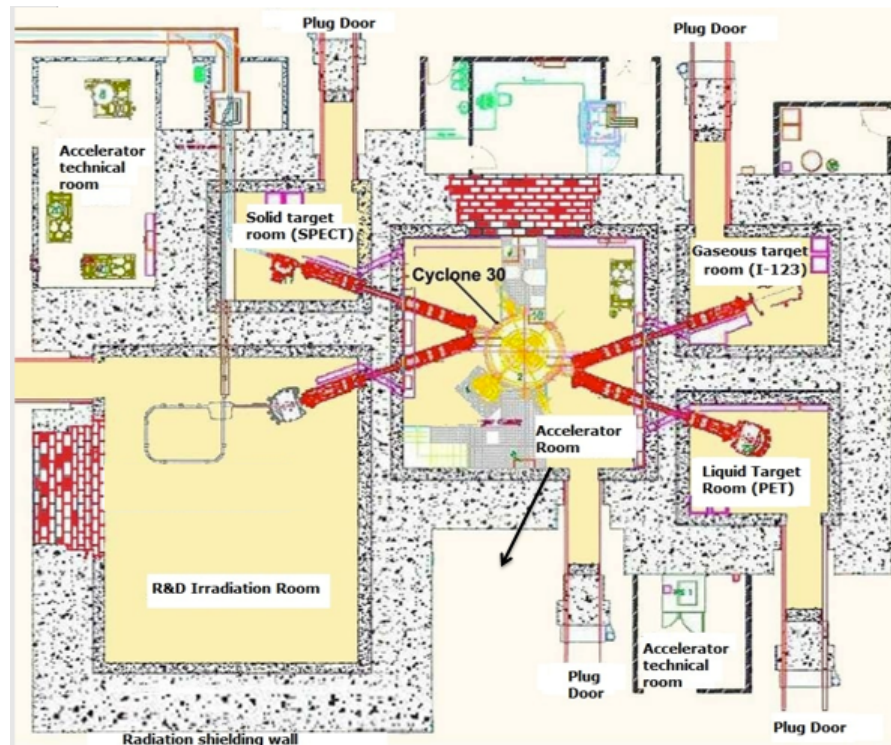
Figure 2.16: 2-D drawing of the TAEA SANAEM Proton Accelerator Facility shows the cyclotron and four rooms. At center of the facility, a cyclotron is located that can accelerate protons up to a kinetic energy ranging from 15 MeV to 30 MeV. Four irradiation rooms are available in the facility for different purposes. Three of them are used for production of radioisotopes and later to be chemically converted into radiopharmaceuticals. A fourth and larger room is reserved for R&D experiments.

Beam parameter ranges at the end of the current irradiation lines are shown in Table 2.8. METU-ESRAP (Experimental Space Radiation and Astroparticle Physics Group) is constructing a defocusing beamline that will be located in the R&D room

Table2.8: TAEA SANAEM Proton Accelerator Facility (PAF) Beam Properties.

The Energy Range	15 MeV-30 MeV
The Current Range	0.1μA-1.2 mA
The Beam Size at R&D room	1 cm circle

of the TAEA SANAEM PAF [53]. A target area at the end of the beamline will satisfy the requirements of ESA-ESCC No:25100 standard, seen in Table 2.9. Electronics and materials under this radiation environment will be tested against some types of Single Event Effects. For the nominal design of METU-DBL, a 30 MeV beam is selected to have the deepest penetration depth possible. The beam must be enlarged to the size required by the standard and for SEEs the flux range and uniformity studied carefully [54].

Table2.9: Ranges of energy and flux acceptable under the requirements of the ESA-ESCC No:25100 standard and the required beam size and uniformity for SEE tests.

Parameters	Value
The energy range	20 MeV - 200 MeV
The flux range	10^5 p/cm^2/s to at least 10^8 p/cm^2/s
The beam size	15.40 cm $\times$ 21.55 cm
The uniformity	$\pm$ 10 %

Test methods during proton irradiation tests is also given in the ESA-ESCC 25100 standard. The device under test must be normal to the beam axis for proton tests in the acceptable energy range. Fluxes must be compatible with the response time of the device under test and the speed of test hardware and software. Fluence must total 10^{11} protons/cm^2 by the end of the proton tests at the target area according to this standard. Nearly 5 exposures at different energies between 20 to 200 MeV are required to plot a response curve. One example for a typical response curve for heavy ions can be seen in Figure 2.17. The device SEE sensitivity can be characterized with its cross section (σ) curve. This curve can be plotted when the device is irradiated with protons or heavy ions. There are no SEEs below the threshold LET and saturation cross section (σ_{sat}) is the total area of sensitive parts of the device. [55]

28
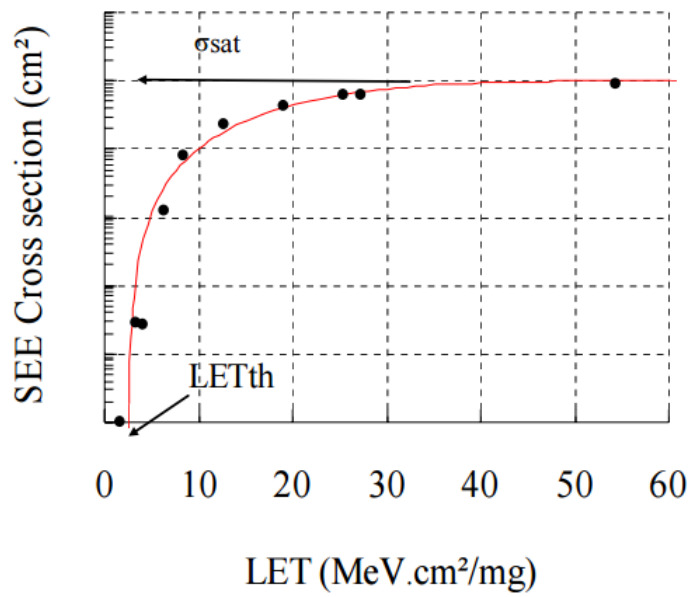
Figure 2.17: SEE Cross Section Curve versus particle LET or proton energy shows the characterization of SEEs sensitivity of a device. Below threshold LET, SEEs can not occur and saturation cross section (σ_{sat}) is the total area of sensitive parts of the device [55].

However, accumulated total dose or displacement damage can often degrade the SEE response. To measure the effect of the device degradation over test time, electrical parameters of the device such as supply current must be monitored and also reference tests must be frequently performed during the SEE test. If the total dose is significant, new samples must be available during the tests. Also, the standard suggests performing total ionising dose test before the SEE test. If the device is particularly sensitive to the total ionising dose, a larger number of samples can be prepared in advance for the SEE test [7]. Proton irradiation time is dependent on flux selected to reach the required fluence.

The proton beam available at the TAEK SANAEM PAF has nearly one cm radius and its minimum flux setting is 0.1 μA in the R&D room. The limitation of using an energy at the low end of the range allowed by the standard is that only one card or component can be tested at a time; meaning they can not be stacked behind one another unlike at IRRAD facility at CERN [49]. Protons with 30 MeV kinetic energy can penetrate only 5 mm in Silicon material, seen in Figure 2.18.
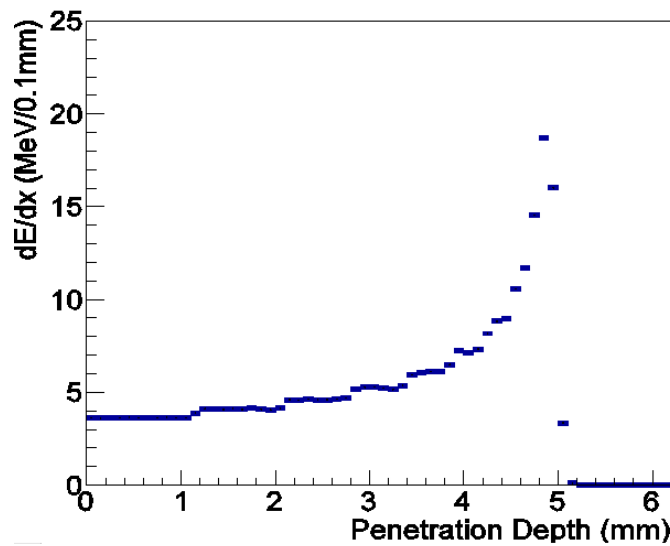
Figure 2.18: Bragg Curve shows the penetration depth of 30 MeV protons in a silicon sample as simulated in GEANT4. It can penetrate 5 mm in the silicon. [56].

Although the kinetic energy of proton beam (15-30 MeV) is suitable according to the standard, the beam size is small and the beam flux is rather high. Thus, the beam must be enlarged to increase the proton beam size and collimated to decrease the flux of

the proton beam so that it can satisfy the ESA-ESCC 25100 standard. The uniformity of the beam must also be between $\pm$ 10 % at the target area. To reach these requirements, quadrupole magnets and scattering foils are used to enlarge the beam size and collimators with different apertures and shapes are designed to decrease the number of particles.
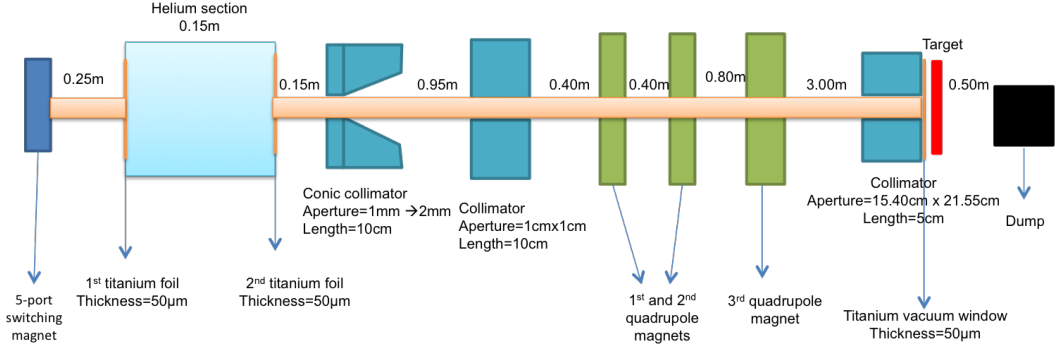
Figure 2.19: METU-DBL final design includes quadrupole magnets and scattering foils to enlarge the beam size, collimators to reduce the number of particles and a window at the end of the beamline for the beam to exit vacuum.
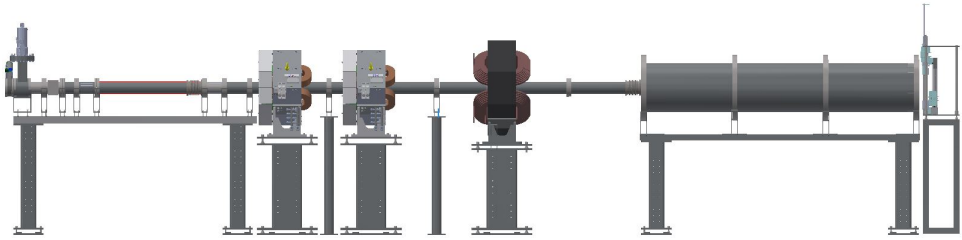
Figure 2.20: The 3-D technical drawing of the final design of METU-DBL includes quadrupole magnets and scattering foils to enlarge the beam size, collimators to reduce the number of particles and a window at the end of the beamline for the beam to exit vacuum. The beam pipes, the vacuum flanges, the support tables of pipes and the target area systems are drawn here in scale.

Design considerations and choices will be discussed in detail in the next chapter. The current METU-DBL design can be seen in Figure 2.19 [57] and its 3-D technical drawing can be also seen in Figure 2.20 [58]. The 3-D technical drawing of the final design of METU-DBL includes three quadrupole magnets and scattering foils to enlarge the beam size, collimators to reduce the number of particles and a window at

the end of the beamline for the beam to exit vacuum. The beam pipes, the vacuum flanges, the support tables of pipes and the target area systems are drawn with actual their measures in detail. METU-DBL will be located after a 5-port switching dipole magnet, which will enable performing different experiments in the same room. The left-most port with respect to the outgoing beam with a 40° bending angle will be used by METU-DBL since it provides the longest possible beamline length. This magnet has been ordered from IBA [59] and it will arrive and be commissioned at the TAEK SANAEM PAF around the end of 2017. During this time, a pretest set-up will be constructed to gain operational experience and to test some equipment and components in conditions similar to that of the standard and common in literature. Two quadrupole magnets, a collimator and a Ti vacuum window will be used. The METU-DBL pretest set-up is under construction and will be commissioned in spring 2017.

When a beamline is designed, results from two different simulation program are often compared to increase the reliability of the design. For the METU-DBL project design, the TRANSPORT and MAD-X programs are used for beam optics. In addition, G4beamline and TURTLE have been selected to track particles and control beam parameters at every critical point. In the following chapter, the considerations studied and results of G4beamline simulation for the METU-DBL project will be presented in detail.

CHAPTER 3

G4BEAMLINE SIMULATIONS FOR THE METU DEFOCUSING BEAMLINE AND IRRADIATION AREA

The G4beamline program is a useful and steadily improving tool to effectively model beam dynamics and experimental equipment around it. It has both graphical and command line user interfaces, as it is based on the Geant4 toolkit. Unlike most accelerator physics codes, it easily handles a wide range of materials and electric and magnetic fields [60].

In this chapter, basic definition of some properties in accelerator physics will be presented. Later, simulations and comparisons with TURTLE of each critical point in METU-DBL will be given. Secondary particles, prompt dose from these particles and beam dump studies will be also included in this section. In the following section, collimator design studies to protect quadrupole magnets from the beam halo will be presented in detail. In the final section, final beam parameters will be shown for the pretest set-up that is currently under construction.

3.1 Basic Concepts of a G4beamline Simulation

3.1.1 Definition of Beam Parameters

A particle beam can be defined in terms of beam emittance and phase space properties of the beam. Emittance (ϵ) characterizes a beam's size and corresponds to an elliptical area in the phase space of the particles. The direction of a particle's motion, defined by "s" , is perpendicular to x and y directions, as shown in Figure 3.1. The

phase space variable pairs for a particle are (x, x_p) and (y, y_p) with time as an independent variable. These coordinates correspond to the position (x, y) and momentum (x_p, y_p) components of the particle [61]. In addition to these parameters, there are correlations, represented by r, between position and momentum in x and y directions, that give the phase space distributions in these directions.
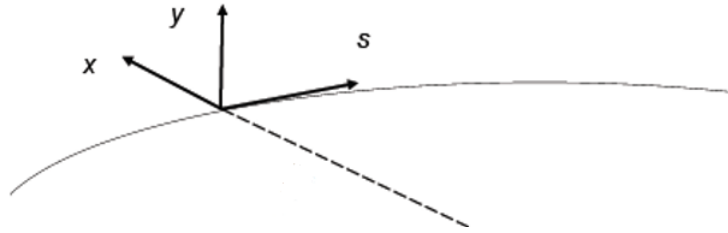
Figure 3.1: The direction of a particle's motion is represented by "s" in accelerator physics. x and y directions are perpendicular to it.

The distribution of particles in the phase space is often taken to be a Gaussian distribution in each position and momentum coordinates. The area of the ellipse in each direction, which corresponds to the emittance, remains a constant unless a disruptive element such a collimator or a scattering foil is in the beam. However, the shape of ellipse can change along the beamline, as shown in Figure 3.2.

3.1.2 Working Principles of Beam Elements

Commonly used beam elements in a non-accelerating beamline can be listed as dipole and quadrupole magnets, foils and collimators. An understanding of their specific functionalities is necessary to assess how they affect beam parameters. Beam profile, energy or intensity can be modified after entering a beam element. These effects which result from the equation of motion of the particle can be calculated with matrices [62].

Lorentz Force on a particle in an electric field, $\vec{E}$ and a magnetic field, $\vec{B}$, seen in Equation 3.1, represents the equation motion of the particle [63]. Beam dynamics for particles passing through a quadrupole or a dipole magnet can be derived from this
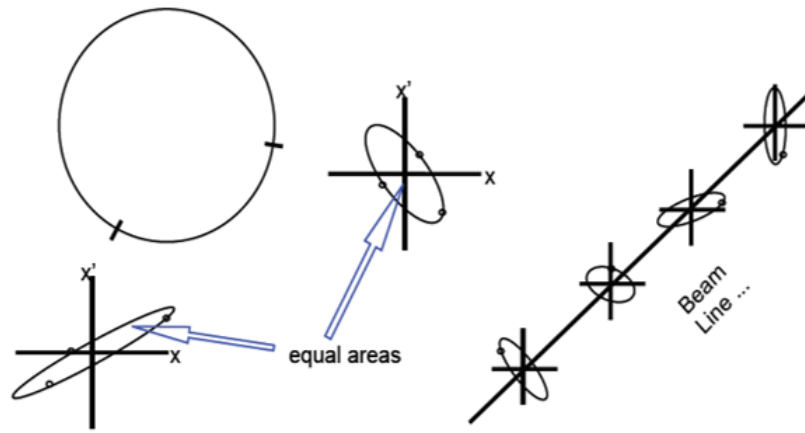
Figure 3.2: The area of the ellipse in each direction, which corresponds to emittance, remains a constant unless a disruptive element such a collimator or a scattering foil is in the beam. However, the shape of phase space ellipse can change along the beamline [61].

formula.

$$\overrightarrow{F} = q(\overrightarrow{E} + \overrightarrow{v} \times \overrightarrow{B})$$ (3.1)

A dipole magnet, often called a bending magnet, applies a dipole field on a charged particle so that the particle can be bent in one axis. If B is a constant magnetic field, its bending strength for a particle with charge q, called magnetic rigidity R, can be expressed as:

$$R = B\rho = \frac{p}{q}$$ (3.2)

where ρ is the bending radius and p is the particle momentum [64].

Dipole magnets can be classified according to their shapes as sector, edge, total bend or rectangular [65]. These can be explained as the following:

- Sector Dipole Magnet: magnetic field lines are perpendicular to the incoming and outgoing trajectory of a particle

- Edge Dipole Magnet: the faces of the magnet are perpendicular to the trajectory at the entrance and the exit.

- Total Bend Magnet: the faces of the magnet have arbitrary edge angles at the entrance and the exit.

35

- Rectangular Bending Magnet: in the bending plane, each edge acts as a defocusing lens.

Both dipole magnets used in METU-DBL are sector magnets. Two simulation programs, used in the design of METU-DBL, have different dipole definitions. TURTLE models the fringe fields of sector dipole magnets while G4beamline does not. This will be discussed in Section 3.2 in detail.

A quadrupole magnet consists of four poles. When a quadrupole magnet focuses a beam in one direction, it defocuses the beam in the other direction, as seen in Figure 3.3. Conventionally, a quadrupole magnet can be classified according to its focusing or defocusing properties on particles. If a quadrupole magnet focuses the beam in x, while defocusing the particles along y, it is called a focusing magnet. Otherwise, it is called a defocusing magnet. At the center of the magnet, there is no net force on particles. However, it applies a force on a particle proportional to the distance to the center of the magnet because the field lines are denser near the edges of the magnet [64]. When two quadrupole magnets, called a quadrupole doublet, are used, the beam size can be enlarged in both axes by the end of this doublet.
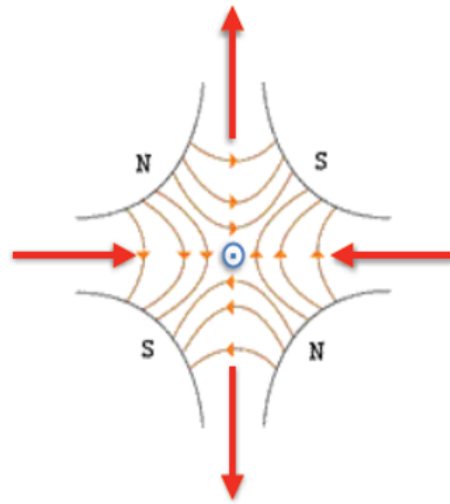
Figure 3.3: A quadrupole magnet has four poles. Field lines of such a magnet can be seen in the figure. When a quadrupole magnet focuses a beam in one direction, it defocuses the beam in the other direction.

While magnets are often used to change the beam direction and size, different beam elements such as foils and collimators can be employed to reduce the number of parti-

cles per unit area per second, called flux. Foil is a thin material that scatters particles; therefore, it is called a scattering foil. Particles passing through matter suffer repeated elastic Coulomb scattering from nuclei however with a small probability. Considering that nuclei in the material often have a greater mass than the incoming particle, the energy transfer is negligible, but each scattering centre adds a small deviation to the incoming particle's trajectory. Even if this deflection is small, the sum of all contributions adds a random component to the particle's path, that is called as a zig-zag path, shown in Figure 3.4. Therefore, after the incoming beam passes through some thickness of material, the final divergence is greater than the initial [66]. For multiple scattering, as the thickness increases and the number of interactions become high and the angular dispersion can be expressed as a Gaussian distribution.
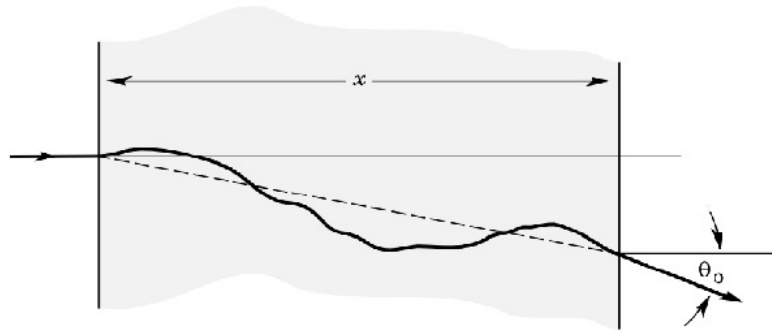
Figure 3.4: Effect of multiple Coulomb scattering on the incident particle on a plane. Since a nucleus in the material often has a greater mass than the incoming particle, each scattering centre adds a small deviation to the incoming particle's trajectory. Even if this deflection is small, the sum of all contributions adds a random component to the particle's path, that is called as a zig-zag path [67].

For the METU-DBL project, multiple Coulomb scattering calculations from G4beamline will be presented in the Section 3.2.2. In addition, a particle also losses some of its energy when it passes through a foil. If the thickness of the foil is enough to stop some particles in the kinetic energy distribution, the beam flux can also be decreased.

A collimator must be thick enough to stop particles so that it can reduce the number of particles in the beam and through the hole in the middle, give the beam the desired shape by cutting the halo. Using the beam elements mentioned above, the flux, shape and energy of a beam can be adjusted to obtain the desired parameters at the target

area. To ensure proper functioning of a beamline including beam elements, at least two reliable simulation programs must be used to predict and check the beam profile, energy and the number of particle. Here G4beamline will be used and compared with results from TURTLE.

3.2 G4beamline Simulations for the METU Defocusing Beam Line

3.2.1 Defining the Initial Beam Profile for the METU-DBL

The cyclotron in the Proton Accelerator Facility (PAF) can produce protons between 15 and 30 MeV kinetic energy. The average momentum of 30 MeV protons is 239.2 MeV/c, as calculated from Equation 3.3 where m_p is the proton mass and ke is the kinetic energy of the proton.

$$P = \sqrt{(m_p + ke)^2 - (m_p)^2} \tag{3.3}$$

The cyclotron's extracted beam has a $\pm 1\%$ energy dispersion and momentum has a similar dispersion. The kinetic energy of particles at the end of the beamline needs to be in the range defined in the ESA-ESCC No:25100 standard, which means that the lowest allowable energy for SEE tests is 20 MeV. As it is easier to bend lower energy particles, all beam dynamics and magnet studies are done for 30 MeV, unless explicitly stated.

In the G4beamline program, energy dispersion can easily be defined for the initial beam and the generated energy spectrum can be seen in Figure 3.5. The generated spectrum has a 1σ of 0.3 MeV as expected. Also, the generated momentum spectrum of the initial particles can be seen in Figure 3.6. The observed 1σ of this distribution is 1.22 MeV/c around a central momentum of 239.2 MeV/c.

One dipole and 4 quadrupole magnets steer the beam from the exit of the cyclotron into the R&D room. After these elements, a 5-port switching (dipole) magnet will be placed at the end of the available beamline. This magnet will allow having five different experimental stations in the R&D room. The METU-DBL starts at the end of this 5-port switching magnet. Here, the results of the G4beamline simulations for METU-DBL elements will be presented in detail.
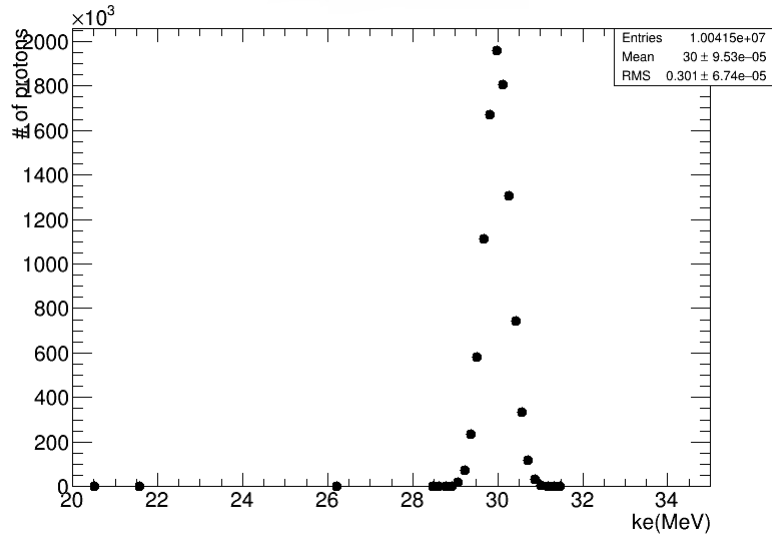
Figure 3.5: The energy distribution of an initial 30 MeV protons with the $\pm 1\%$ dispersion at the beginning of METU-DBL.

The parameters of the initial beam coming out of the cyclotron are obtained from the available TRANSPORT code [68]. Initial beam extracted from the cyclotron is a rotated ellipse in both $x - x_p$ and in $y - y_p$ planes, where the 1σ distributions are given in Table 3.1. The beam distribution is defined using the 1σ of the distribution around the average value of 0.

Table3.1: Initial 1σ beam parameters, σ_x, σ_y for position and σ_{x_p}, σ_{y_p} for momenta for a 30 MeV beam, just after extracting the beam from the cyclotron. Correlations between position and momentum, represented by r, are given as r_{x,x_p} for x and r_{y,y_p} for y.

σ_x	4.20 mm
σ_{x_p}	1.37 mrad
r_{x,x_p}	0.897
σ_y	3.16 mm
σ_{y_p}	3.13 mrad
r_{y,y_p}	0

Two independent particle tracking programs are necessary to prove the reliability and the robustness of the design. For the METU-DBL project, the G4beamline and TUR-TLE [69] programs are used to track the motion and to analyze the trajectories of

39
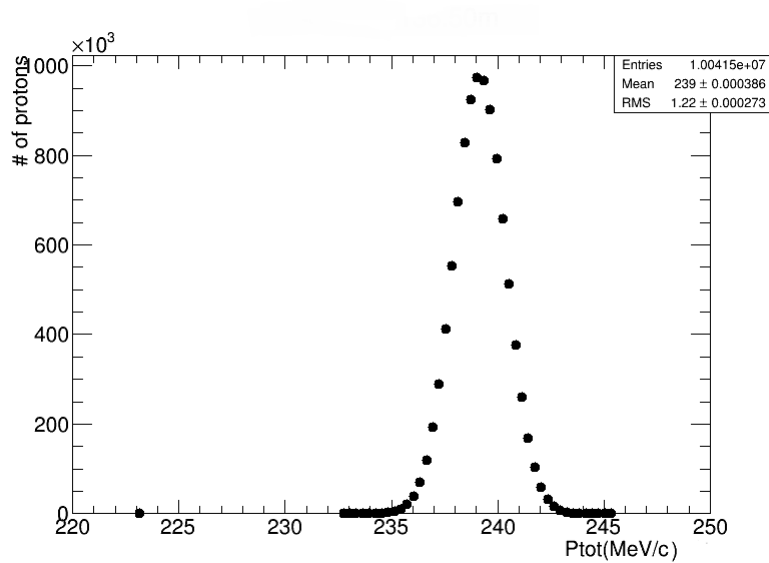
Figure 3.6: The momentum distribution of 30 MeV initial beam with the $\pm 1\%$ dispersion at the beginning of METU-DBL. The momentum distribution is centred around 239.2 MeV/c and 1σ is 1.22 MeV/c for this case.

particles along the beamline. In G4beamline, available beam elements are defined, as seen in Figure 3.7. However, it defines dipoles differently than TURTLE as mentioned in Section 3.2. For this purpose, the beam up to the end of the 5-port switching magnet was only simulated in TURTLE and parameters at that point are used as input for the following G4beamline studies for the sake of comparison.
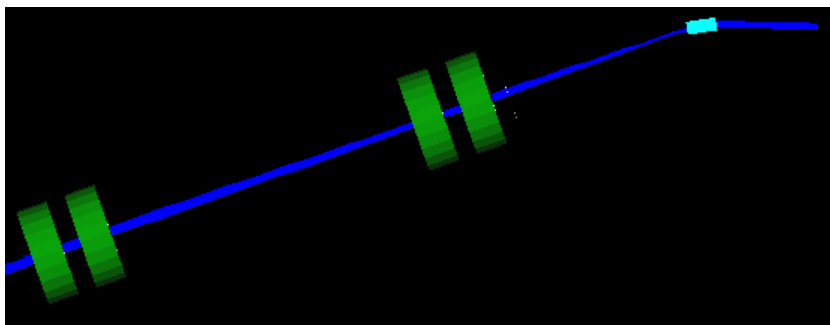
Figure 3.7: The visual output of a G4beamline simulation for beam elements starting from the exit of the cyclotron in the R&D room.

The initial 1σ beam parameters after the 5-port switching magnet obtained from TURTLE, which are σ_x and σ_y for positions, σ_{x_p} and σ_{y_p} for momenta of particles and correlations in both planes, $x - x_p$ and $y - y_p$, are given in Table 3.2.

Table3.2: Initial beam parameters σ_x, σ_y for position σ_{x_p}, σ_{y_p} for momenta for METU-DBL after the second dipole magnet. Correlations between position and momentum, represented by r, are given like r_{x,x_p} for x and r_{y,y_p} for y.

σ_x	8.66 mm
σ_{x_p}	5.19 mrad
r_{x,x_p}	0.9397
σ_y	2.78 mm
σ_{y_p}	6.30 mrad
r_{y,y_p}	-0.9646

Correlations can easily be defined in TURTLE but the definition is not readily available in the G4beamline program. Thus, a macro code, written in the C++ [70], re-assigns the initially generated particles in the beam to the correlated momentum in G4beamline to obtain the correlated ellipse distributions in $x - x_p$ and $y - y_p$ planes. Representation of beam ellipses from the TRANSPORT manual [71] are employed for this reassignment. To ensure that the obtained ellipse matches the TURTLE output, the phase spaces for both $x - x_p$ and $y - y_p$ planes from two programs are compared, as seen in Graphs 3.8 and 3.9 for TURTLE and G4beamline respectively. While the ellipse in $x - x_p$ plane, obtained from G4beamline, has tails, there is no tail in the corresponding ellipse from TURTLE. The collimator cuts the tails of distribution in TURTLE while not effecting the general distribution parameters that are taken as input to G4beamline. However, this does not result in a discrepancy since these tails are cut by collimators that follow this initial point in the METU-DBL design.

3.2.2 Foils and Helium Chamber Studies

The beam size at the end of the 5-port switching dipole magnet is nearly circular with a diameter of 1 cm and the current was initially taken to be the lowest measurable setting of 10 μA. The corresponding flux is nearly 2×10^{11} p/cm^2/s and its distribution is not uniform to $\pm$ 10 % as required by the ESA-ESCC No:25100 standard. However, the flux must take a value from 10^5 p/cm^2/s to at least 10^8 p/cm^2/s and also the beam area must be 15.40 cm $\times$ 21.55 cm, to satisfy the ESA-ESCC No:25100 standard. The required uniformity can be satisfied by expanding the peak of the beam
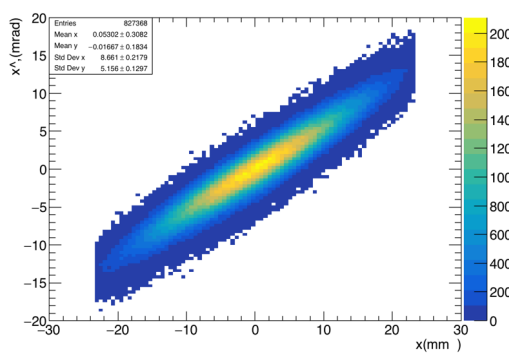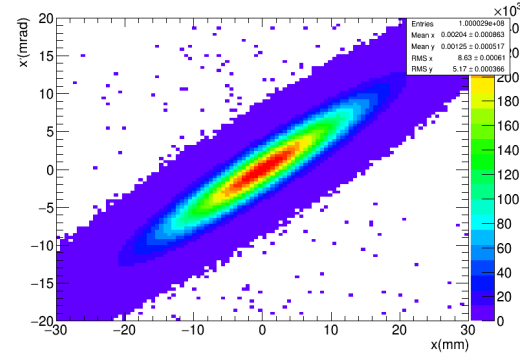
<div style="text-align:center">(a) TURTLE   (b) G4beamline</div>

Figure 3.8: Phase space graphs in the $x - x_p$ plane from both TURTLE and G4beamline at the beginning of METU-DBL,While the ellipse in $x - x_p$ plane, obtained from G4beamline, has tails, there is no tail in the corresponding ellipse from TURTLE. The collimator cuts the tails of distribution in TURTLE while not effecting the general distribution parameters that are taken as input to G4beamline. However, this does not result in a discrepancy since these tails are cut by collimators that follow this initial point in the METU-DBL design.

distribution to the full area of the target and cutting the tails. Therefore, the beam must be first enlarged or scattered. For this purpose, two thin foils are used to scatter the particles and decrease the flux. A cold helium section, which also adds to the scattering effect, is necessary to cool these scattering foils which are exposed to a high particle flux. This section also provides a natural separation between the vacuum system of the available beam line and METU-DBL. Beam energy, momentum and other parameters here will be analysed for various scattering foil thicknesses and helium section lengths.

Material for scattering thin foils is selected as titanium due to its high heat-resistance compared to other materials. Tungsten also has a high heat-resistance, but more energy is lost in tungsten when compared titanium, as seen in Table 3.3. Energy loss is kept to a minimum to allow the proton beam to reach the target with the maximum energy. Thus, titanium is selected as the material to scatter the particles.

The stability of a current less than 10 μA could not be measured with the available beam instruments at TAEA SANAEM PAF. In this case, two titanium foils with 150

(a) TURTLE	(b) G4beamline
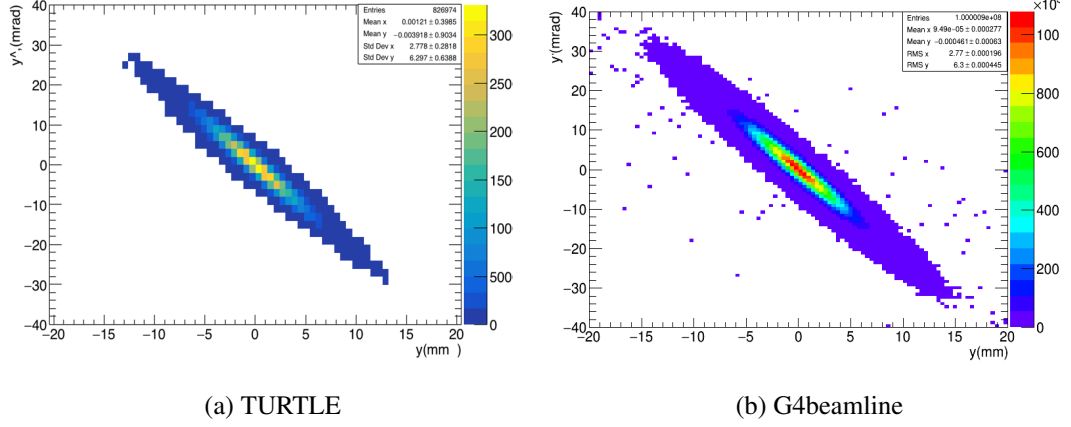
Figure 3.9: Phase space graphs in the $y - y_p$ plane from both TURTLE and G4beamline at the beginning of METU-DBL.While the ellipse in $y - y_p$ plane, obtained from G4beamline, has small tails, there is no tail in the corresponding ellipse from TURTLE. However, this does not result in a discrepancy since these tails are cut by collimators that follow this initial point in the METU-DBL design.

Table3.3: Energy deposition in titanium and tungsten foils with 150 μm thickness and final kinetic energy of a protons with 30 MeV after two foils.

Material	Energy Deposition in 150 μm length	Final Kinetic Energy
Titanium	0.9 MeV	29.1 MeV
Tungsten	2.6 MeV	27.4 MeV

μm thickness would be used to have a minimal energy loss while scattering particles sufficiently. Later, a special sensitive camera was deployed by the METU-DBL team and it was observed that the lowest accelerator setting of 0.1 μA also provides a stable beam current. Therefore, different length settings for the foils and the helium section here are considered. A cold helium section between scattering foils provides cooling for the foils when they are exposed to protons and also helps to scatter the protons. For the 10 μA setting, a length of 25 cm would be enough to cool them.

Energy and dispersion studies and comparisons are performed using foils with 150 μm and thinner foils with 50 μm thickness because multiples of 50 μm are commercially available. The cooling requirement necessarily decreases for thinner foils and the helium cooling section length is decreased to 15 cm for the study of 50 μm foils.

When designing a cooling system, the worst case scenario for an initial current of 100 μA and 30 MeV kinetic energy proton beam is considered. The power lost in a 50 μm thickness Ti foil can be calculated by using Equation 3.4. In this equation, I is current, l is the thickness of the Ti foil and ρ is the density of Ti which is 4.54 g/cm^3. The stopping power can be calculated from the Bethe-Bloch formula and is 12.8 MeV·cm^2/g in this case.

$$P(W) = I(\mu A) \times l(cm) \times \rho \left(\frac{g}{cm^3} \right) \times Stopping Power \left(\frac{MeV \times cm^2}{g} \right) \quad (3.4)$$

The power lost in the first Ti foil is 29 W and the second foil is 29.4 W. Lost power will heat the titanium foils and can easily be removed. The helium section will be surrounded by the beam pipe and will be cooled in two ways: by circulating cooled helium and by a water cooling jacket around the beam pipe.

Bethe-Bloch Formula defined in Section 2.3 and Multiple Coulomb Scattering mentioned in Subsection 3.1.1 can explain the physics of how the beam scattering changes with increasing thickness. Thicker foils cause more energy loss in the material and then particles scatter more. To examine how Ti foil thickness affects the beam parameters, a pencil beam, with zero size, is sent to the Ti foils with 150 μm and 50 μm thickness using different He section lengths. A comparison of the results in Table 3.4 shows that after the second Ti foil, the beam size is nearly three times larger if 150 μm foils and 25 cm cooling section are used. When the 0.1-1 μA current is used, thinner foils can be used to get the same final flux after an appropriately sized collimator. Therefore, the Ti foil thickness is selected as 50 μm and helium cooling section with 15 cm length is enough when 0.1-1 μA current is used for METU-DBL. In addition, this choice provides less energy loss for protons with the beam leaving this scattering section with 29.36 MeV instead of the alternative 28.13 MeV, as shown in Table 3.5, therefore increasing the energy range of METU-DBL. A larger energy range can increase the available spectrum.

After pencil beam studies, a realistic study of the existing beam is simulated. Comparison of the beam parameters for the selected configuration before and after this scattering section is performed and can be seen in Table 3.6. The beam size has increased slightly while the σ_{x_p} and σ_{y_p} have more than doubled. A long flight path after this section will enlarge the beam more and allow for selecting the core of the

Table3.4: The beam parameter are compared for different foil thickness (l) and different He section length (d).

After Section	Parameters	σ_x(mm)	σ_{x_p}(mrad)	σ_y(mm)	σ_{y_p}(mrad)
1st Ti foil	l=50μm	0.01	6.80	0.1	7.00
	l=150μm	0.02	12.1	0.2	11.9
1st Ti foil + He section	l=50μm,d=15cm	1.1	6.7	1.2	6.8
	l=150μm,d=25cm	3.2	12.3	3.3	11.7
1st Ti foil + He + 2nd Ti foil	l=50μm,d=15cm	1.2	10.1	1.2	9.79
	l=150μm,d=25cm	3.3	17.7	3.2	16.9

Table3.5: Kinetic energy after each foil 50 μm and 150 μm thicknesses and helium section with 15 cm and 25 cm lengths.

Kinetic Energy After	1^{st}Foil	He Section	2nd Foil
50 μm foils and 15 cm He section	29.71 MeV	29.66 MeV	29.36 MeV
150 μm foils and 25 cm He section	29.11 MeV	29.04 MeV	28.13 MeV

beam with a collimator.

Table3.6: Beam parameters σ_x, σ_y for position σ_{x_p}, σ_{y_p} for momenta before and after two foils with 50μm thickness and 15 cm He section in between.

Parameter	Before Foils & He Section	After Foils & He Section
σ_x	11.1 mm	12 mm
σ_{x_p}	5.17 mrad	13.2 mrad
σ_y	0.87 mm	2.28 mm
σ_{y_p}	6.32 mrad	13.7 mrad

3.2.3 Conic Collimator Studies

After scattering particles, the halo of the beam must be eliminated to decrease the number of particles so that the core of the particle distribution can satisfy the required flux and uniformity at the target area. For this purpose, a conic collimator is placed after the titanium scattering foils and helium cooling section. Particles, hitting outside

of the collimator aperture, lose their energy and stop after losing all of their energy. Particles inside the acceptance region reach the end of collimator without losing any energy in the vacuum. Collimators with different apertures can be placed on a rotating system to provide the desired flux at the target location. The range of interchangeable apertures will be from 1 mm to 10 mm. It can eliminate a different number of particles with different apertures, as seen in Table 3.7.

Table3.7: The percentage of eliminated particles after the conic collimator with different aperture settings.

Aperture	Percentage of eliminated particles
$1 \rightarrow 2$ mm	99.66%
$2 \rightarrow 3$ mm	99.21%
$3 \rightarrow 4$ mm	98.46%
$4 \rightarrow 5$ mm	97.42%
$5 \rightarrow 6$ mm	96.14%
$6 \rightarrow 7$ mm	94.54%
$7 \rightarrow 8$ mm	92.82%
$8 \rightarrow 9$ mm	90.97%
$9 \rightarrow 10$ mm	88.93%

In this section, alignment of beam elements, especially for smallest aperture, is critical to satisfy the desired parameters at the target area. The beam and beam elements are shifted from their nominal positions to analyse how possible alignment problems may affect the beam parameters at the target area. Statistics is limited to an initial 2.1×10^9 particles in the G4beamline program which makes it difficult to prove the ± 10 % uniformity at the target area, but is enough to study the effects of the shifted beam on the uniformity. First, beam alignment studies for the conic collimator with the smallest aperture, 1 mm aperture, is performed with the shifted beam in only one direction when all beam elements are located nominally. Results of how much uniformity is affected by shifting the beam by 1 mm in the x direction can be seen in Table 3.8.

If the beam is shifted by even 1 mm, the uniformity at the desired target area are affected significantly. The $\pm 10\%$ uniformity requirement for the ESA-ESCC No:25100 standard in both axes can be lost at the target area. Thus, the center of the proton beam

Table3.8: The uniformity of the shifted beam with the initially 10^8 protons by 1mm at the target area for both axis compared with the nominal beam.

Uniformity	X axis	Y axis
Without shifted beam	6.1 %	8.5 %
With shifted beam by 1 mm	7.5 %	10.2 %

coming from the cyclotron must be monitored continuously. During irradiation tests, temperature changes on collimators will be monitored. An increase can indicate that the center of the beam is shifted. If so, the beam stopper can be activated by the control system to stop the beam.

3.2.4   Final Beam Elements

After the scattering foils, the helium cooling section and the conic collimator, three quadrupole magnets, two additional collimators, one to protect a magnet and another to define the irradiation area at METU-DBL are placed. The beam then exits through a vacuum window (50 μm Ti) and hits a beam dump if there is no sample being tested.

The three quadrupole magnets enlarge the beam to satisfy the beam size requirement of the ESA-ESCC No:25100 standard. Two of them have been procured from the Scanditronix as a standard commercial product, as shown in Figure 3.10 and they have the same physical parameters, seen in Table 3.9. The definition of these physical parameters of a quadrupole magnet in G4beamline are shown in Figure 3.11.

Figure 3.10: Two commercial quadrupole magnets procured from the Scanditronix.

Table3.9: The parameters of two commercial quadrupole magnets procured from the Scanditronix.

Pole Tip Radius	55 mm
Coil Half Width	22.4 mm
Coil Radius	78.26 mm
Iron Radius	217.5 mm
Field Length	290 mm
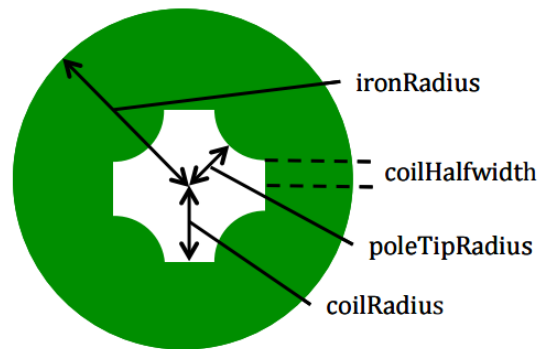
Figure 3.11: The definition of physical parameters of a quadrupole magnet as input to a G4beamline simulation [72].

The last and the third quadrupole magnet is under a call for tenders since it is not commercially produced. It has a strong magnetic field; therefore, has been especially designed for METU-DBL. The magnetic field strength of the three quadrupole magnets are determined and are shown in Table 3.10 in units of kiloGauss (kG) [57]. Conventionally, a positive magnetic strength represents a focusing quadrupole magnet and a negative sign indicates a defocusing quadrupole magnet. The G4beamline simulation program can define quadrupole magnets in detail by using these parameters.

The first collimator, located before the first quadrupole magnet in METU-DBL, is placed to protect the magnet from particles scattered from the exit of the conic collimator. Quadrupole magnets can be faced with some mechanical or electrical problems when they are exposed to these particles if they are not protected. The other

Table3.10: The magnetic field strength of quadrupole magnets used in METU-DBL shown in units of kiloGauss(kG). 1kG is equal to 0.1 Tesla.

Beam Element	Magnetic Field Strength
1. Quadrupole Magnet	3.3 kG
2. Quadrupole Magnet	-1.2 kG
3. Quadrupole Magnet	-6.5 kG

collimator, located after the last quadrupole and just before the vacuum window, is used for defining the desired beam size at the target area according to the ESA-ESCC No:25100 standard. These two collimator parameters can be seen in Table 3.11.

Table3.11: Collimator parameters located before the first and after the third quadrupole magnet of METU-DBL.

Collimator	Aperture size	Length
Before quadrupole magnets	1 cm x 1 cm	10 cm
After quadrupole magnets	15.40 cm x 21.55 cm	5 cm

The proton beam must move in vacuum inside a beamline so that the interactions between protons and molecules in the beam volume can be as little as possible. Hermetically sealed beam pipes are used to conserve the vacuum of the METU-DBL system. The vacuum must be better than 10^{-5} mbar because the cyclotron control system in the PAF stops if the beam in the vacuum is worse than this value. For the METU-DBL, the vacuum system is designed at the 10^{-6} mbar level, which is in the ultra-high vacuum (UHV) range. At the end of the beamline, a vacuum window is also placed to withstand the pressure difference between the vacuum inside and the air outside the METU-DBL.

Material selection of these elements is also a critical point for METU-DBL. Due to the interaction of particles with the materials, secondary particles can be produced during irradiation and they can create a high level dose rate in the R&D room and even activation in some beam elements, that are directly exposed to these particles. This can affect the durability and service time of these elements. Thus, materials used for critical elements such as the collimators, beam pipes and the beam dump,

49

are selected from special industry standard materials used for space and accelerator applications. Selected materials for these beam elements can be seen in Table 3.12. Dimensions of the collimators, the foils, the beam pipe and the beam dump system can be also seen in Table 3.12 where ρ is a diameter and d is a length or a thickness of a beam element.

Table3.12: Used materials and dimensions for collimators, beam pipes, foils and beam dump system of the METU-DBL where ρ is a diameter and d is a length or a thickness of a beam element.

Type	Element	Dimension	Material
Collimators	Conic	Outer ρ=10 cm	Stainless Steel 316
	1st coll		
	2nd coll	Outer ρ=40 cm	
Beam pipe	Upto 1 m away of the exit of 3rd magnet	Inner ρ=9.8 cm	
		Outer ρ=10 cm	
	Upto window	Inner ρ=37.5 cm	
		Outer ρ=40 cm	
Foil	1st foil	d=50μm	Titanium
	2nd foil		
	Window		
Beam Dump	Cover	d=2 mm	Graphite
	Stopping Volume	d=12 cm	Aluminium 6082

The beam dump system and parameters will be detailed in Section 3.2.7. Beam pipe of the METU-DBL is also necessary for a realistic simulation. The beam pipe is widened from 10 cm to 40 cm about 1 m after the 3rd quadrupole magnet since the beam is enlarged. The G4beamline simulation representation of all beam elements and beam pipe is shown in Figure 3.14. In the output, the proton beam comes from left inside the beam pipe shown in grey. Green rectangle represents a quadrupole magnet, red is a collimator and purple is the helium chamber surrounded by Ti scattering foils. White rectangle is the beam dump located at the end of METU-DBL. For this design, the beam profile at the target area and the corresponding beam energy distribution can be seen in Figure 3.12 obtained by using a conic collimator with the smallest aperture (1 $\rightarrow$ 2 mm) and in Figure 3.13 obtained by using a conic collimator with the biggest aperture (9 $\rightarrow$ 10 mm).

(a) Final Beam Profile (b) Final KE Distribution

Figure 3.12: Final beam profile and kinetic energy distribution at the target area of the METU-DBL by using the conic collimator with the smallest aperture widening from 1 mm to 2 mm. 10^8 protons is sent from the start of METU-DBL for this simulation.

3.2.5 Secondary Particle Studies Produced by the METU-DBL

When five different experimental stations are installed in the R &D room of TAEA SANAEM PAF, during an irradiation, the experiment being conducted will create some secondary particles and increase the dose rate in the room. This increased dose can affect elements or components of other experimental stations, especially if they contain sensitive devices. Thus, the dose rate needs to be limited to protect experiments and their components in the R&D room. Currently, TAEA SANAEM PAF has not issued such a limit for experiments conducted in the room.

In the METU-DBL system, secondary particles are produced by the halo of the beam hitting elements of the beamline or on the collimators or by the core of the beam at the target area and at beam dump. Thus, the background dose rate in the R&D room will increase during irradiations and remain high for some time after the irradiation due to free neutrons and activation of materials. Therefore, secondary particles, their kinetic energy at production and the generated flux are examined to predict the dose rate created by the entirety of METU-DBL and to design a shielding system for reducing the dose rate in the room.

When particles are fired into a block of material, the collisions between the incoming particle and particles in the material create a multitude of secondary particles. Parti-

51

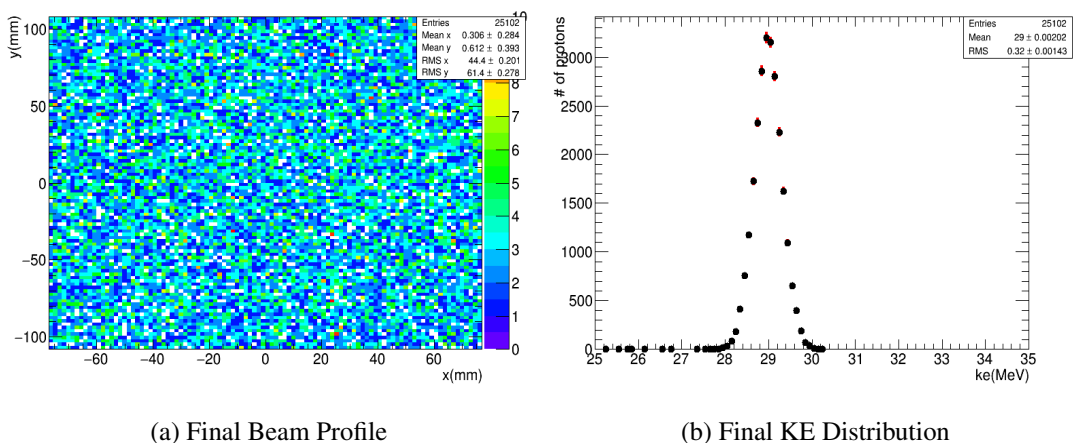(a) Final Beam Profile   (b) Final KE Distribution
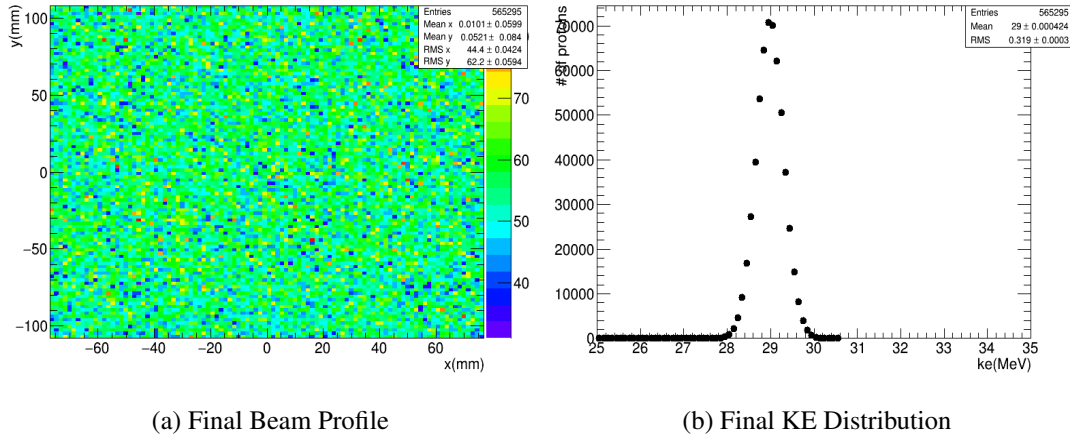
Figure 3.13: Final beam profile and kinetic energy distribution at the target area of the METU-DBL by using a conic collimator with the biggest aperture widening from 9 mm to 10 mm. 10^8 protons is sent from the start of METU-DBL for this simulation.

cles (nuclei and electrons) in the material have different energies and move randomly in all directions. Every collision creates a different type of secondary particle with a different kinetic energy generated by different physical processes. For example, in facilities working with heavy particles with high energy, many secondary particles are created by nucleus-nucleus interactions. These particles, especially neutrons, can produce radioisotopes in the accelerator materials, cooling air or water. They can also penetrate through the building of the facility into the surrounding environment. Thus, evaluating the emission of secondary particles and the creation of the residual nuclei in various materials is necessary [73].

Various parts of METU-DBL will also create secondary particles. 30 MeV protons are not high enough energy to create pions or muons, common in other accelerator environments, but is still high enough to free neutrons from nuclei or create or scatter hard-electrons or create gammas. These produced particles can be easily identified in the G4beamline program because it gives the ID of the particle, using the assigned value from the Particle Data Group, called PDGID [74]. Also, it can output the track identifier for each track's parent, called ParentID. By using these tags, particles produced as secondaries and the elements that created them can easily be examined in detail [72]. Also secondary particles can be visually identified from the G4beamline simulation representation if an initial 1000 particles (the limit for visual output) are

52
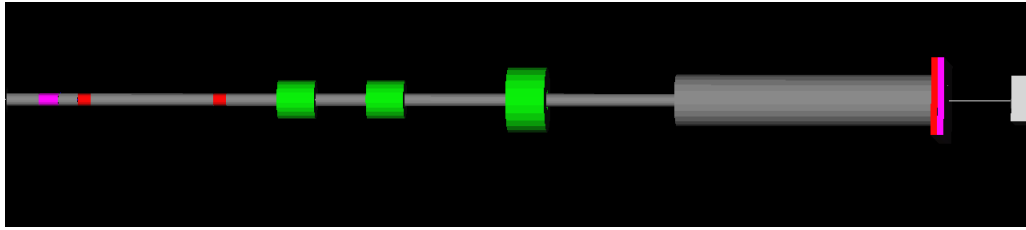
Figure 3.14: G4beamline simulation representation of all beam elements and also dump system. The proton beam comes from left inside of the beam pipe shown in grey. Green is quadrupole magnet, red is a collimator and purple is the helium chamber surrounded by Ti scattering foils. White rectangle is beam dump at the end of METU-DBL.

statistically enough to create secondaries. G4beamline simulation visual output in Figure 3.15 includes all beam elements and also the dump system and shows the secondary particles produced from the conic collimator and the foil and helium section for an initial sample of 1000 protons. Electrons, in grey, are mostly created by foils and the helium section while neutrons, in red, and gammas, in green, are produced from collimators.
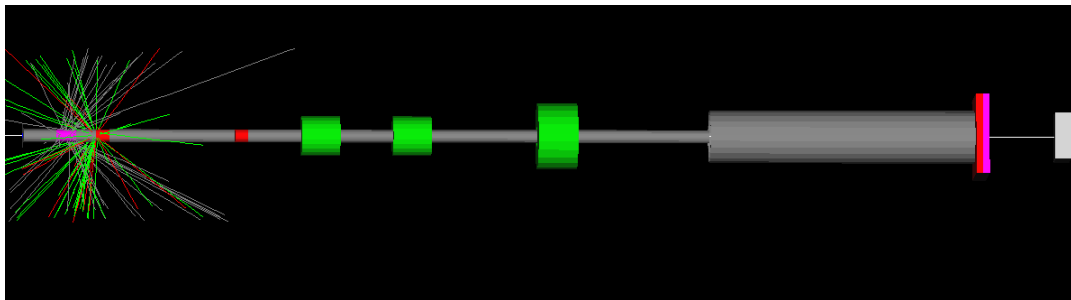
Figure 3.15: G4beamline visual output showing the secondary particle production in METU-DBL. The proton beam comes from left side of the design. Grey rays are electrons generated from the foil and helium cooling section, red rays are neutrons and green lines represent gammas. They can be statistically produced from the initial 1000 proton, that is a limit for the output.

To examine the secondary particles in detail, rectangular and circular detectors are defined around, before and after beam elements in G4beamline and this simulation is repeated using higher statistics. The secondary particle analysis to determine critical parts of the METU-DBL can be seen in Table 3.13. By using the data obtained from

the virtual detectors covering one side of a critical part, the kinetic energy ranges of secondaries are obtained, as seen in Figure3.16 (a) for gammas, (b) for electrons and (c) for neutrons. The average kinetic energy of the produced gammas are 2.7 keV but the distribution has a long tail that extends to 80 keV. The average electron is similar in energy to an ionized electron, with the average of the distribution at 11 eV but with a tail that extends to 25 keV, from rare hard-scatters. Neutrons are the most energetic secondaries with an average of 1.7 MeV and have a tail that extends to 25 MeV.

Table3.13: Some sections in METU-DBL are called critical sections due to produce secondary particles. Gammas and neutrons are created by collimators and helium section produces electrons.

Element	Secondary Particle
Helium cooling section	Electron
Collimators	Gamma & Neutron

Before prompt dose calculations and shielding can be studied, user cases must be discussed to understand initial particle rates.

3.2.6 User Cases

The PAF cyclotron can produce a proton beam with an energy range from 15 MeV to 30 MeV. The proton beam coming from the cyclotron losses some energy along the METU-DBL due to interaction with the foils, the helium section, the window and the air volume between the window and the target area. The proton beam reaching the target transfers its energy to the material. Its LET value depends on the beam energy and material it interacts with. Irradiated components are often made of silicon, and here the LET is calculated here for 100 μm thickness silicon. Initial energy, final energy after METU-DBL and their LET values in Si can be seen in Table 3.14. These energies and LET calculated for 100 μm thickness silicon can be provided for users at the target area for users.

After the exit of METU-DBL, SEE tests must be performed in air and some space is necessary for beam diagnostics before the target. In this air volume, protons lose
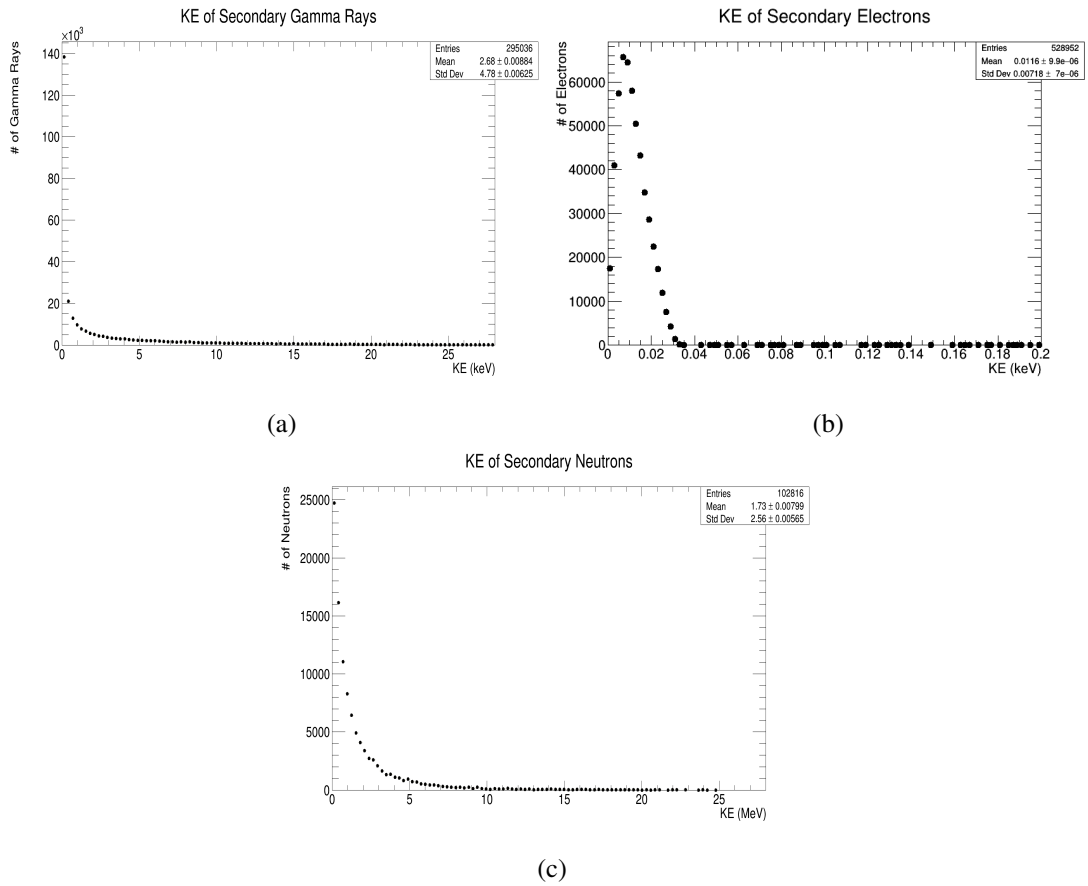
Figure 3.16: Kinetic energy distributions of secondary particles produced in critical parts of METU-DBL. a, b and c are the kinetic energy distributions for gammas, electrons and neutrons respectively. These particles are produced with the initial 10^7 protons.

Table3.14: Final energy after METU-DBL and LET values in 100 μm thickness of Si for various initial energies of the proton beam.

Initial Energy (MeV)	Final Energy at the target (MeV)	LET in Si (MeV cm^2/gr)
30	29	0.15
25	23.8	0.18
20	18.6	0.22
15	13.2	0.28

some of their kinetic energy due to interaction with molecules of air. Therefore, this length is designed to be as small as possible.

The METU-DBL system can also allow for providing different fluxes by changing the conic collimator's aperture and the initial current and different energies at the target area. With flexible irradiation parameters, METU-DBL can provide an irradiation area at the target, which can be used for different purposes. Predicted common user scenarios can be seen in Table 3.15.

Table3.15: Different currents, energies and conic collimator apertures for different irradiation purposes in METU-DBL.

Possible Scenarios				
Scenarios	Current	Conic Collimator	Energy	Purpose
A	1 μA	1 $\rightarrow$ 2 mm	15 MeV	Solar Panel Tests
B	1 μA	1 $\rightarrow$ 2 mm	30 MeV	Preliminary SEE Tests
C	1 μA	9 $\rightarrow$ 10 mm	30 MeV	Nominal SEE Tests (ESA-ESCC No:25100)
D	100 μA	9 $\rightarrow$ 10 mm	30 MeV	High Luminosity LHC Tests

As a part of the METU-DBL project, the solar cell of the IMECE satellite will be tested to examine its radiation tolerance. Proton irradiation tests for a solar cell is often performed with a 10 MeV proton beam and these tests must be realized in vacuum or in a dry atmosphere of nitrogen or argon to protect them from oxidation [40]. In the TAEA SANAEM PAF, the minimum kinetic energy extracted from the accelerator is 15 MeV. To obtain a proton beam with 10 MeV kinetic energy, a energy degradation

system must be added to the METU-DBL. A vacuum chamber or a chamber filled with a dry atmosphere of nitrogen or argon will be placed at the end of METU-DBL in which a solar cell will be irradiated and some foils will be placed in front to decrease the kinetic energy to 10 MeV. This degradation system will be studied later in detail. Each solar cell can be tested with an equivalent flux that it will be exposed to space. In this case, the flux that IMECE's solar cells will receive is considered in SPENVIS. SPENVIS gives the damage equivalent fluence for a defined solar cell in a defined orbit. If a cover glass with a 100 μm thickness is used, the equivalent 10 MeV proton fluence is 10^{10} p/cm^2. This fluence should be reached in scenario A.

Innovative components, which are developed for space applications, can be irradiated with a low flux of protons during one hour. The irradiation with a low flux during a limited duration is critical to determine the radiation tolerance of new components, as in scenario B. For this reason, a conic collimator aperture widening from 1 mm to 2 mm can be used to provide a low flux at the target area. If irradiation time is considered as one hour, 3×10^9 p/cm^2 fluence is reached at the target area in one hour.

Components, where rad-hardness or radiation-tolerance are required, need to be tested with a high flux to reach the desired fluence in the ESA-ESCC No:25100 standard in reasonable irradiation time. According to the standard, the fluence of 10^{11} p/cm^2 must be reached for SEE tests. If a conic collimator with an aperture widening from 9 mm to 10 mm is used with an initial 1 μA current, this fluence is reached at the target area after 1.4 hours. This type of tests here are called Nominal SEE tests, in scenario C.

High Luminosity LHC tests can be also performed by using METU-DBL. These tests require a neutron fluence of 10^{14} p/cm^2, which is equivalent to a proton fluence of 4.3 $\times 10^{13}$ p/cm^2. To reach this high fluence at the target area in a possible shortest time, a conic collimator aperture from 9 mm to 10 mm can be used with an initial 100 μA current. This fluence can be satisfied after 6 hours of irradiation but can be slower to satisfy the requirement that fluxes must be compatible with the response time of the device under test. The cooling system of METU-DBL is designed for a maximum current of 100 μA but cooling of the sample needs to be considered carefully.

Possible scenarios mentioned above will require different irradiation durations depending on the required fluence. The desired fluences, provided fluxes and expected

test times can be seen in Table 3.16 for each of the cases considered here. A test sheet will be prepared for users to provide details about the possible beam parameters at the target area. For this purpose, three beam diagnostics are being prepared to be installed just before the target area. Beam diagnostics which are an array of fiber scintillators, a pixel detector and a diamond detector will be moved in both axes to scan the target area and measure the energy and uniformity of the beam profile.

Table3.16: Required fluences for possible irradiation scenarios, fluxes and testing times.

Possible Scenarios			
Scenarios	Flux	Fluence	Test time
A	8.3×10^5 p/cm^2/s	10^{10} p/cm^2	1 hour
B	8.3×10^5 p/cm^2/s	3×10^9 p/cm^2	1 hour
C	1.9×10^7 p/cm^2/s	10^{11} p/cm^2	1.4 hours
D	1.9×10^9 p/cm^2/s	4.3×10^{13} p/cm^2	6 hours

3.2.7   Prompt Dose Calculations for Some User Cases and Beam Dump Studies

Interaction of energetic primary particles and various materials generate radiation, which may be separated into prompt and residual radiation. Prompt radiation is defined as initial or instantaneous radiation. It consists of secondary particles produced within a second of the irradiation by the primary particles [75]. Residual nuclei surviving longer than a second at the interaction site can be radioactive and is called residual radiation. Here the G4beamline simulation of prompt dose will be presented. Residual radiation will be studied using FLUKA in a separate work package.

The G4beamline simulation program gives the total energy deposition in MeV per second by the command $totalenergy$, which prints the total energy deposited in a defined volume. This absorbed energy given by " MeV per second " can be converted to " Joule per second " by using the relation 3.5 to perform a dose calculation. The common unit of absorbed dose by a material is usually expressed as " rad ", and is

58

defined as 0.01 J/kg.

$$1 MeV = 1.6 \times 10^{-13} Joule \tag{3.5}$$

Air volumes around the critical beam elements must be defined to calculate the prompt dose, given from the METU-DBL system to the R&D room. Helium section, scattering foils and collimators are defined as critical parts and air volumes around them are defined as well, as seen in Figure 3.17. Air volumes start from the surfaces of the critical beam elements extend to a distance one meter away.
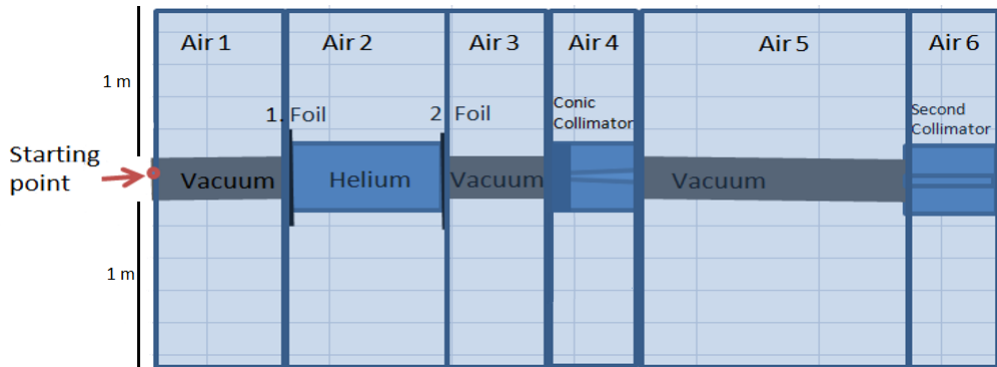
Figure 3.17: Schematic showing the air volume considered around critical beam elements. A volume that starts from the surface of a critical beam element and expands one meter away is defined to calculate the prompt dose in air.

The prompt dose rate levels during the operation of METU-DBL are calculated for the most likely scenarios for different apertures and currents without any shielding, as seen in Table 3.15. The prompt dose rate for the scenarios B, C and D are calculated during their foreseen test duration, without any consideration for activation in materials or in air. These rates are rather high and these critical elements must be shielded to reduce the prompt dose in the room.

Table3.17: Prompt doses for possible different irradiation scenarios for METU-DBL.

Scenarios	Conic Collimator Aperture	Current	Prompt Dose
B	1 mm → 2 mm	1 μA	70.4 rad/h
C	9 mm →10 mm	1 μA	93.8 rad/test
D	9 mm →10 mm	100 μA	40.2 krad/test

Radiation on the target area must mostly consist of protons with $\pm$ 10 % uniformity to ensure the reliability and accuracy of the irradiation tests. Some secondaries produced by other elements in the beamline can change the test conditions and confuse test results. Especially particles arriving from beam elements, located just before and after the target area, are difficult to discern from primaries. A beam dump must be located at the end of the beamline to stop the beam and to prevent scattering of the beam from the wall of the room. The beam dump must be long enough to stop all protons while limiting the creation of secondary particles. To analyse secondary particles, virtual detectors are placed just before the dump. Then, the beam dump is removed while the detector remains in the same location. The comparison of these configurations show that secondaries are produced on the front face of the dump. These particles are called "Backscattered Particles". Backscattering is defined as the deflection of radiation or particles by electromagnetic or nuclear forces through angles greater than 90° to the initial direction of travel. When particles interact with matter, some of them can experience backscattering. To examine backscattered particles, a silicon sample with 2 mm thickness covers the target area and a visual detector with the same area follows the sample. Then, scenarios with different distances between the target and the dump are studied. The dump can be covered to reduce the number of secondary particles coming from the dump to target area. The results of studies can be seen in Table 3.18. An initial sample of 10^7 protons are examined in these studies. The number of particles and direction of secondary particles detected by the detector just after the target area can be seen. Best choice to protect the target area from secondaries is a dump system with 12 cm of aluminium covered with 2 mm of graphite.

The beam dump system, where the number of back-scattered particles is kept to a minimum, can be seen in Figure 3.18. This dump system is used for both the METU-DBL and METU-DBL pretests.

3.3   G4beamline Simulations for Pretests of METU-DBL

Until a 5-port switching magnet is commissioned in R&D room, a pretest set-up will be constructed by using the available quadrupole magnets, a collimator, a beam pipe and also a vacuum window to gain experience in testing some components. This

Table3.18: Different dump system configurations are studied by changing the distance between the target and the dump. The dump can also be covered with graphite to reduce the number of secondary particles coming from the dump to the target area.

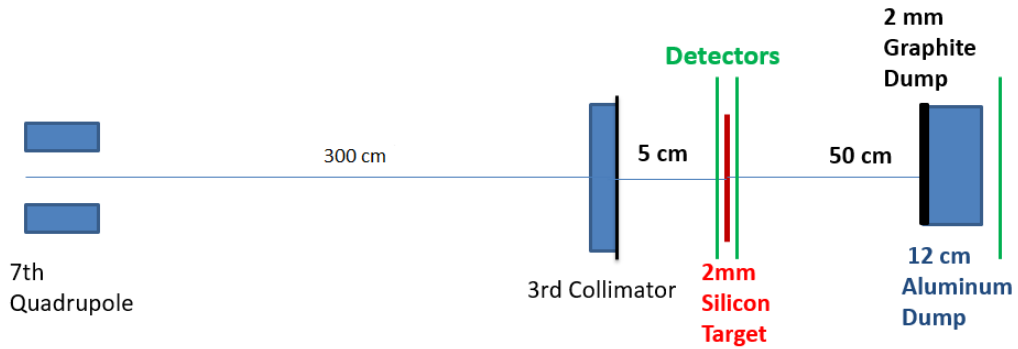| Dump	Distance between dump and target	Number and direction of		
		electron	gamma	neutron
12 cm Al	20 cm	→171	→1	→7
		←84	←37	←2
12 cm Al	50 cm	→159	→2	→1
		←60	←34	←0
12 cm Al+ 2 mm graphite	50 cm	→159	→2	→1
		←52	←19	←0

Figure 3.18: Final beam elements of METU-DBL and the beam dump system.

design starts from the end of a 4-jaw collimator, which is already located after the four quadrupole magnets leading to the R&D room, as seen in Figure 3.19. The beam element parameters for the pretest can be seen in Table 3.19 [57]. A quadrupole doublet structure extrudes the wall, followed by a solenoid magnet, which will not be activated in METU-DBL. A beam viewer and a vacuum shutter follow along the beamline. A 4-jaw collimator is currently the final element, but will be removed when the 5-port switching magnet arrives.

Pretest will be the preliminary study for METU-DBL and there is no extra budget for this engineering step allocated in the project. Thus, some parts such as the beam pipe or the collimator in the pretest are those planned for METU-DBL to reduce the cost of the pretest. In this design, the drifts between the collimator and the second dipole are the same with drifts in METU-DBL to use the same beam pipes.

Figure 3.19: The available beam elements in the R&D room. A quadrupole doublet structure extrudes the wall, followed by a solenoid magnet, which will not be used in METU-DBL. A beam viewer and a vacuum dumps follow along the beamline. A 4-jaw collimator is currently the final element, but will be removed when the 5-port switching magnet arrives.

3.3.1 Defining the Initial Beam for the METU-DBL Pretest

The initial parameters obtained from TURTLE for the METU-DBL pretest setup are σ_x and σ_y for positions, σ_{x_p} and σ_{y_p} for momenta of particles and correlations on both two planes, $x - x_p$ and $y - y_p$, as seen in Table 3.20.

Since correlations are not readily available in the G4beamline program, the generated particles are again reassigned in the beam to the correlated momentum in G4beamline to obtain the correlated ellipse distributions in $x - x_p$ and $y - y_p$ planes for the pretest. To ensure that obtained ellipses are correct, phase space graphs on both planes from G4beamline and TURTLE are again compared, on the $x - x_p$ and $y - y_p$ planes as shown respectively Graphs 3.20 and 3.21. The ellipses in $x - x_p$ plane and in $y - y_p$, obtained from G4beamline have tails, but there are no tails in the same ellipses obtained from TURTLE. Because, a 4-jaw collimator cuts the tails of distribution in TURTLE. These tails are later cut by an other collimator, located in the pretest set-up, otherwise they are very similar distributions.

Table3.19: The beam element parameters for the METU-DBL pretest setting.

Collimator	Aperture=1 cm
	Aperture shape=square
	Length=10 cm
1st quadrupole	Aperture=11 cm
	Magnetic field=-0.33 T
2nd quadrupole	Aperture=11 cm
	Magnetic field=0.09 T
Window	Thickness=50 μm

Table3.20: Initial beam parameters for the METU-DBL pretest after the 4-jaw collimator are σ_x, σ_y for position σ_{x_p}, σ_{y_p} for momenta. Correlations between position and momentum, represented by r, are given as r_{x,x_p} for x and r_{y,y_p} for y.

|	
σ_x	6.96 mm
σ_{x_p}	2.55 mrad
r_{x,x_p}	0.88
σ_y	4.28 mm
σ_{y_p}	2.41 mrad
r_{y,y_p}	-0.91

3.3.2 Studies of the Collimator Design to Protect Quadrupole magnets

When particles hit a quadrupole magnet, they can cause some mechanical and functional problems. Thus, the number of particles hitting it must be as low as possible. For this purpose, structure of the collimator is studied in detail to protect the first quadrupole magnet.

This problem does not occur in METU-DBL because a conic collimator located before this collimator significantly reduces the number of particles, seen in Table 3.7, and prevents the particles scattered from this collimator to reach the quadrupole magnets.

Analysis of particles hitting the first quadrupole is performed by using virtual detectors, which cover the front surface of the quadrupole magnet, as seen in Figure 3.22. In the figure, a small virtual detector, called "core det" and represented with
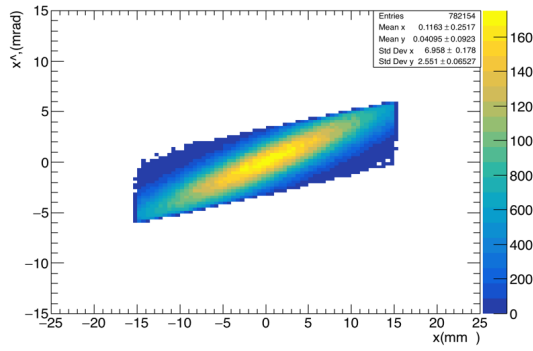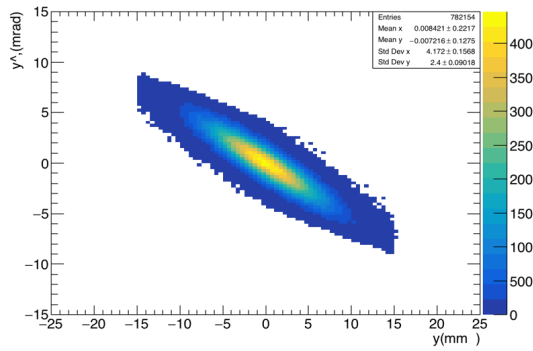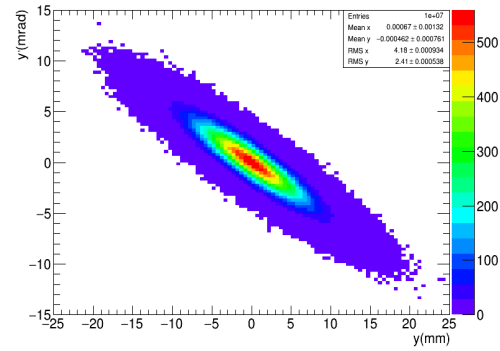
(a) TURTLE
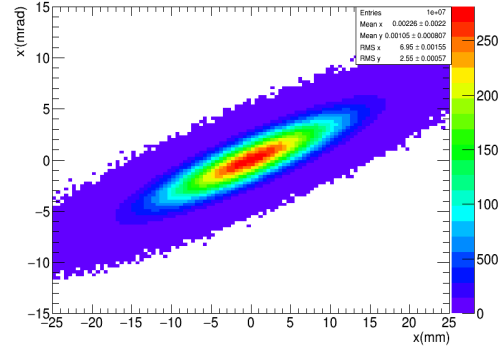
(b) G4beamline

Figure 3.20: Phase space graphs in the $x - x_p$ plane from both TURTLE and G4beamline for METU-DBL pretest.

(a) TURTLE

(b) G4beamline

Figure 3.21: Phase space graphs in the $y - y_p$ plane from both TURTLE and G4beamline for METU-DBL pretest.

a purple area in the figure, has the same size with the core of quadrupole magnet to detect particles hitting it. A bigger virtual detector, called "circumference det" and represented with a grey area in the figure, has the same size with the circumference of the quadrupole magnet to detect particles hitting it. These detectors give how many particles would hit the core or circumference of the quadrupole's face.

To reduce the number of particles hitting the core of the quadrupole's face, the collimator design can be changed or modified with graphite, which reduces back-scatter. Now, collimator design studies are presented in detail.

In METU-DBL and pretest, collimator material is selected as Stainless Steel 316 due
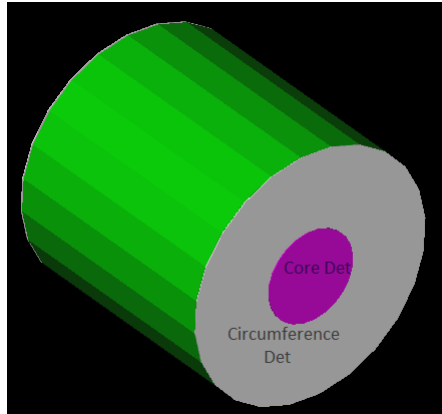
64

Figure 3.22: virtual detectors cover the front surface of the quadrupole magnet. A small virtual detector, called "core det" and represented with a purple area, has the same size with the core of quadrupole magnet to detect particles hitting it. A bigger virtual detector, called "circumference det" and represented with a grey area, has the same size with the circumference of the quadrupole magnet to detect particles hitting it. These detectors give how many particles would hit the core or circumference of the quadrupole's face

to the reasons explained in Section 3.2.4. A sandwich collimator (a), a collimator covered on both sides with 1 mm Graphite (b), a collimator covered inside with 1 mm Graphite (c) and a collimator whose exit is covered with 2 mm graphite (d) are defined in G4beamline and simulation representations for them can be seen in Figure 3.23.

Table3.21: The comparison of the number of particles hitting the inside and outside of the quadrupole magnet is performed for initial samples of 10^7 protons while different collimator designs covered with graphite are studied.

Name	Hitting particles	Inside	outside
a	Sandwich	767	135
b	Collimator covered both sides with graphite	316	39
c	Collimator covered the inside with graphite	206	48
d	Collimator covered the exit side with graphite	258	2

Analysis of the simulation of different collimator designs generates the Table 3.21.

65
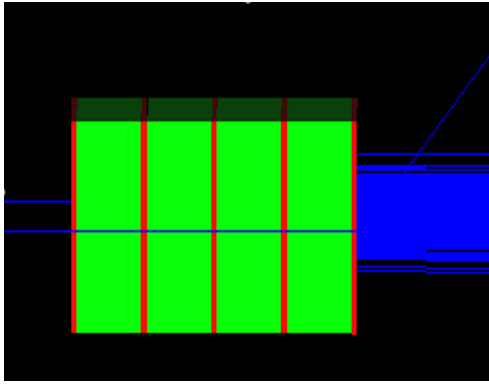
(a) Sandwich Collimator
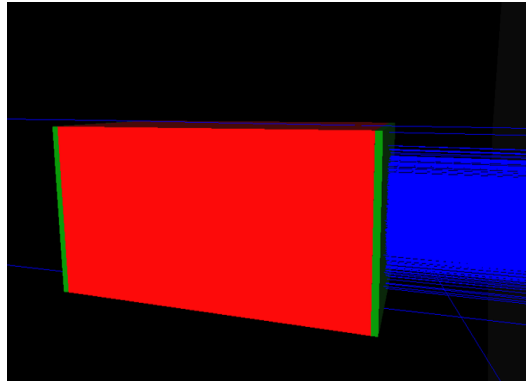
(b) Collimator covered both sides with graphite

(c) Collimator covered inside with graphite

(d) Collimator covered its exit with graphite

Figure 3.23: Different collimators for the METU-DBL pretest are designed to protect the quadrupole magnets from scattered particles. (a)A sandwich collimator has five 2 mm graphite sections which sandwiches 23 mm stainless steel sections. (b)A 10 cm stainless steel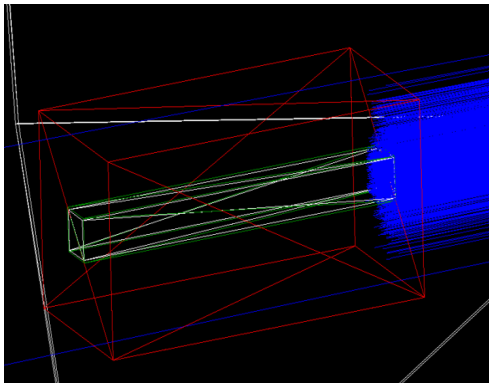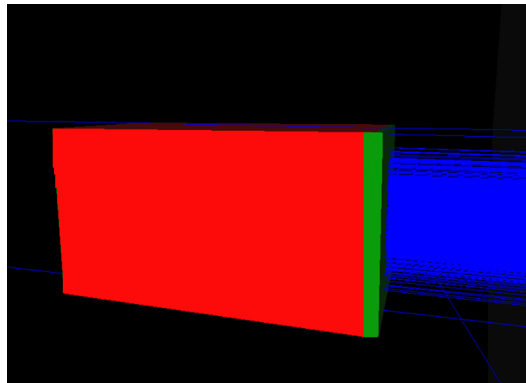 collimator where two ends are covered with 1 mm graphite. (c)A 10 cm stainless steel collimator whose inside is covered with 1 mm graphite. (d) A 10 cm stainless steel collimator whose exits side is covered with 2 mm graphite.

Best choice would be a combination of c and d but the production a collimator whose inside is covered with graphite is difficult; therefore, the configuration where the collimator's exit is covered with 2 mm of graphite is selected for the design of the pretest. The final design for the METU-DBL pretest can be seen in Figure 3.24 [57].

Secondary particles produced on the collimator by the beam is also studied. The G4beamline visual output for secondary particles with initial beam of 1000 protons can be seen in Figure 3.25. In the figure, the proton beam comes in from the left. Red rays are neutrons and green lines represent gammas, which are produced from the collimator. Normally, electrons would also be produced but here the statistics are not
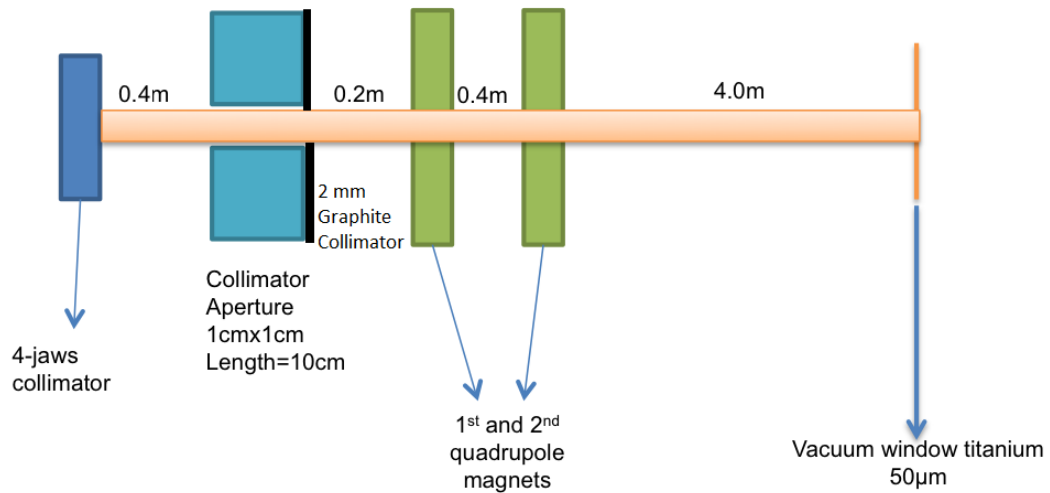
Figure 3.24: The schematic of the final plan for the METU-DBL pretest includes two commercial quadrupole magnets, a collimator with the 2 mm graphite cover to reduce the number of secondary particles and a vacuum window at the end of beam pipe.

sufficient to create them. The energy ranges of secondary particles produced from the collimator are also examined by using a virtual detector around the collimator. The kinetic energy ranges of gammas and electrons can extend into the keV region while neutrons can have energies in the MeV region similar to the results shown in Figure 3.16.

At the target area of METU-DBL pretest, the available beam profile and kinetic energy distribution can be seen in Figure 3.26. The final beam does not have the required size and uniformity of the ESA-ESCC No:25100 standard, but still it has a uniform 6 cm × 2 cm area in its center. This area can provide an irradiation area to perform preliminary SEE tests. The kinetic energy of the final beam is 29.6 MeV and is also suitable for SEE tests.

The 3-D technical drawing for the METU-DBL pretest set-up can be also seen in Figure 3.27 in detail [58]. The 3-D technical drawing of pretest design for the METU-DBL project includes two commercial quadrupole magnets, a collimator to reduce the number of particles and a window at the end of beamline for the beam to exit the vacuum. The beam pipes, the vacuum flanges, the support tables of beam pipes and the target area systems are drawn here to scale in detail.
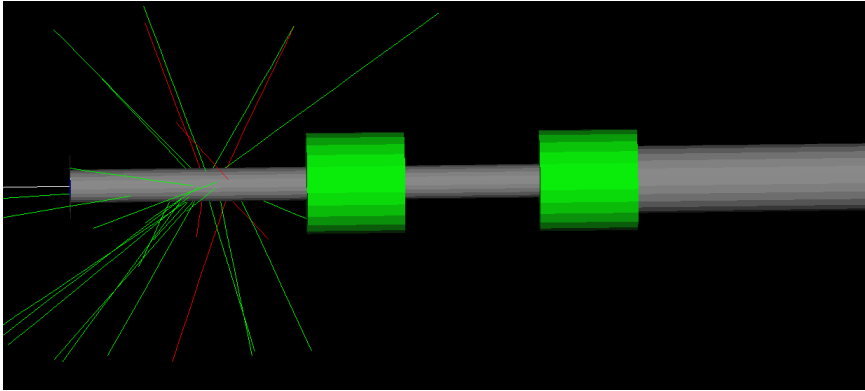
Figure 3.25: G4beamline visual output for the final METU-DBL pretest design is done with protons and produced secondary particles. The proton beam comes from left side of the design. Red rays are neutrons and green lines represent gammas, which are produced from the collimator. Normally, electrons exist as a secondary particle but it can not statistically created with initial 1000 protons, that is a limit for the output.
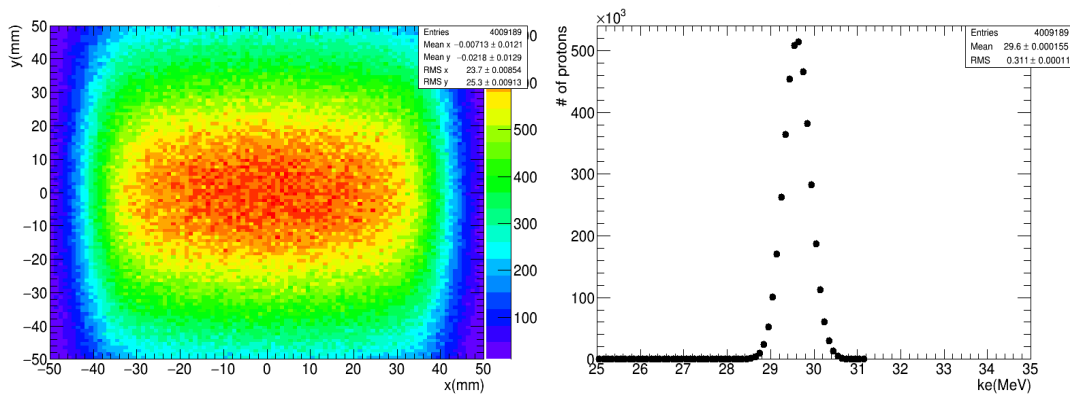
(a) Final Beam Profile

(b) Final KE Distribution

Figure 3.26: Final beam profile and kinetic energy distribution of the METU-DBL are obtained with as sample of 10^8 protons.

Figure 3.27: The 3-D technical drawing of the pretest design for the METU-DBL project includes two commercial quadrupole magnets, a collimator to reduce the number of secondary particles and a vacuum window at the end of beamline for the beam to exit the vacuum. The beam pipes, the vacuum flanges, the support tables of beam pipes and the target area beam diagnostic systems to scale in detail.
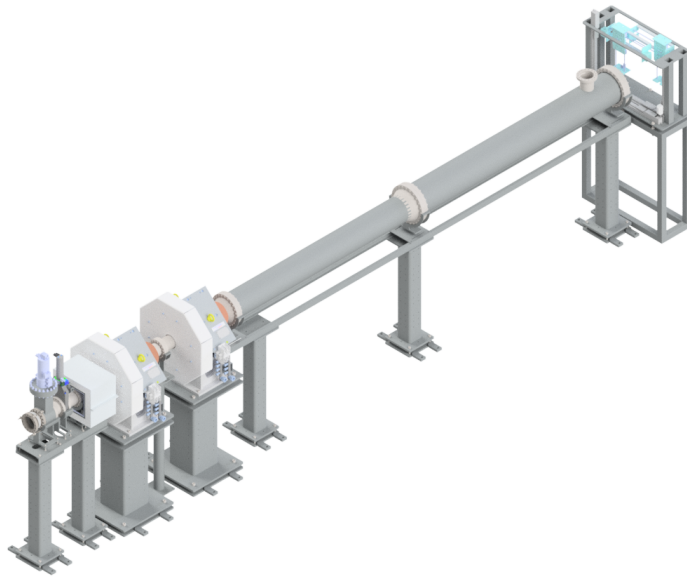
CHAPTER 4

A BEAMLINE DESIGN FOR TESTING DISPLACEMENT DAMAGE EFFECTS ON A ZIRCONIUM SAMPLE USED FOR NUCLEAR APPLICATIONS

Nuclear reactors have a radiation environment in and surrounding their nuclear core which includes energetic particles resulting from fission, radioactive decay products and thermalized particles. Particles such as fast neutrons, protons, alphas, and recoil nuclei interact with the materials around them and can cause production of atomic-scale defects from ballistic collisions and introduction of new chemical elements, called Displacement Damage (DD), mentioned in Section 2.4. The mechanical structure and behaviour of the materials used in nuclear reactors can be changed as a long term effect of this damage [76] These changes can lead to degradation of the mechanical structure and consequently can affect the reliability and the performance of the nuclear reactors [77].

The robustness and performance of materials working under this irradiation environment are critical to increase the reliability of nuclear reactor operations and to decrease production of nuclear waste. Materials inside a nuclear reactor are especially exposed to a high flux of neutrons, causing DD effects [78]. Thus, the neutron cross section of materials is an important consideration in reactors. Zirconium, which has a low absorption cross-section of thermal neutrons, corrosion resistance and high hardness, is often used as cladding of fuel rods in nuclear reactors and the main mechanical component of nuclear fuel assemblies [79]. ^{90}Zr is the most common isotope and constitutes 51.45% of all zirconium on the Earth [80]. The neutron cross-section of the ^{90}Zr isotope can be seen in Figure 4.1 [81].
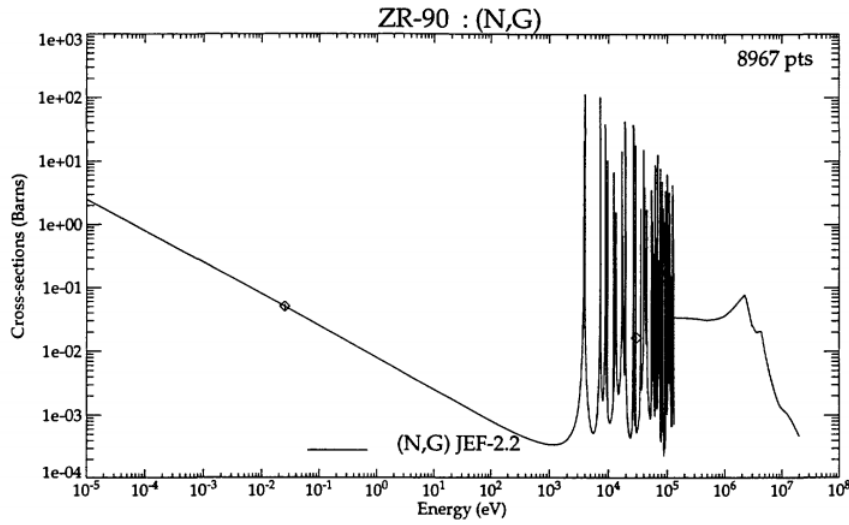
Figure 4.1: The neutron cross-section of the ^{90}Zr isotope [81]

For this purpose, a project has been planned to investigate the effects of nuclear radiation on the mechanical properties of a model zirconium allow, called Zircaloy, under proton and heavy ion irradiation. Analysing the results of DD effects on zirconium alloy material is critical to improving its structure and to qualify it. A grant proposal has been submitted to the Newton-Katip Çelebi call for projects with a collaboration between METU and Oxford University, to transfer knowledge about radiation effects on materials. If accepted, Oxford University will test a zircaloy with heavy ions and METU will perform proton tests on it. After irradiation, the sample's mechanical structure and stability will be analysed with nano indentation and micropillar compression, especially for micro-mechanical cracks and deformations. Then, the results from proton and heavy ions irradiation will be compared. Here, we outline the METU-LEBNA (Low Energy Beamline for Nuclear Applications) proposal to perform proton irradiation tests at the TAEA SANAEM PAF.

The second port of the 5-port switching magnet in the R&D room is considered for the purpose of these tests. If this project is accepted, the available vacuum and cooling systems of the METU-DBL project will be used to build a new adjacent energy degrading beamline to test nuclear materials to the required doses. In this way, the project budget will be reduced. In addition, the knowledge and experience gained during the construction and commissioning of the METU-DBL system will be trans-

ferred to this project due to the similar nature of beamline. The main pre-requirements for proton irradiation tests for nuclear applications can be seen in Table 4.1. Such tests are often performed with a proton beam with 2-3 MeV kinetic energy and the flux irradiating the a sample must be at least 5×10^{13} proton/cm^2/s.

Table4.1: Investigating the effects of nuclear radiation on the mechanical properties of a zirconium sample can be performed using protons with these requirements.

The Proton Kinetic Energy	2-3 MeV
The Flux	5×10^{13} proton/cm^2/s
The Operational Temperature	400^{0}C

In the TAEA SANAEM PAF, the minimum energy setting of the accelerator extraction mechanism is 15 MeV. This energy is rather high to perform this test practically because of the activation of Zr and low nuclear damage rate. Also, micro-mechanical deformations generally form on the surface of the material in nuclear reactors and a 15 MeV proton produces a Bragg peak 700 μm into a Zr sample whereas a 2 MeV proton deposits all of its energy in nearly 40 μm, as seen in Figure 4.2. Therefore, an energy degrading beamline is designed to reach the desired energy range with the initial beam parameters, seen in Table 4.2. Here a focused beam will be the starting requirement of METU-LEBNA to reach a flux as high as possible on the sample. Assuming that METU-LEBNA would have a length of 50 cm (due to technical considerations), optics upstream of METU-LEBNA can be adjusted to have a focal point on the surface of the sample. σ_{x_p} and σ_{y_p} are taken from previous studies and requiring a focal point at the sample, implies that the 1 σ size of the beam at the start needs to be around 1.66 mm. Initial beam profile and kinetic energy distribution with the $\pm 1\%$ dispersion at the exit of the second port of the 5-port switching magnet can be also seen in Figure 4.3.

Titanium foils are used to degrade proton kinetic energy and helium cooling sections with a length of 10 cm are placed between the foils to cool them. Pre-design studies for this system can be seen in Table 4.3. For these studies, the final current and flux incident on the zirconium sample and energy degradation with foils and helium cooling sections are calculated for each trial. Here, an initial current of 100 μA is simulated. The final current is the total current on the 2 cm $\times$ 2 cm Zr sample while
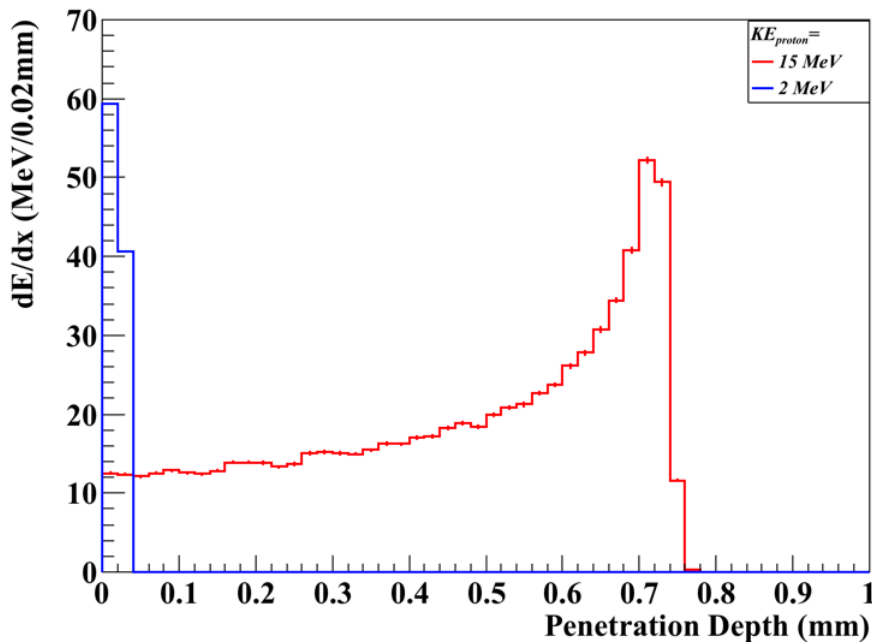
Figure 4.2: The Bragg peaks for 2 MeV and 15 MeV protons.15 MeV produces a Bragg peak 700 μm into a Zr sample whereas a 2 MeV proton deposits all of its energy within nearly 40 μm.

the flux on the central 5 mm $\times$ 5 mm area is quoted. From these trials, the best choice for the design consists of 4 Ti foils with 200 μm thicknesses and 3 helium sections with 10 cm length between the foils. The final beam and kinetic energy distributions on the Zr sample can be seen in Figure 4.4.

For selected design, the G4beamline visual output is used to identify the secondary particles produced by foils and helium sections, seen in Figure 4.5. In the figure, the initial 1000 protons coming from left are represented by blue lines. Three helium sections are shown in magenta and red lines inside these helium sections are the electrons. Green lines are neutrons created on the foils. All beam elements are located inside the beam pipe. In addition, a 3-D technical drawing of METU-LEBNA is shown in detail in Figure 4.6. The beam enters through the left and goes through a beam shutter which can close if the temperature gets too high. Four foils are installed inside flanges and the Zr sample will be placed in a vacuum chamber.

74

Table4.2: Initial beam parameters for the METU-LEBNA project using the second port of the 5-port switching magnet are σ_x, σ_y for position σ_{x_p}, σ_{y_p} for momenta.

σ_x	1.66 mm
σ_{x_p}	3.18 mrad
σ_y	1.66 mm
σ_{y_p}	3.13 mrad

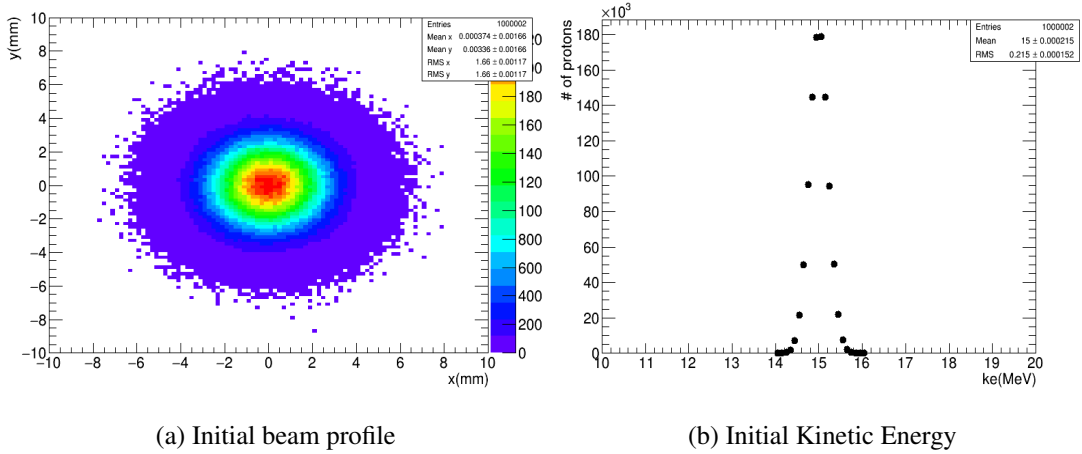(a) Initial beam profile   (b) Initial Kinetic Energy

Figure 4.3: Initial beam profile and kinetic energy for the METU-LEBNA project using the second port of the 5-port switching dipole.

Table4.3: Final current and flux incident on the zirconium sample and energy degradation of several configurations with foils and helium cooling sections. Here, an initial current of 100 μA is simulated. The final current is the total current on the 2 cm × 2 cm Zr sample while the flux on the central 5 mm × 5 mm area is quoted here.

Used Foil Numbers and Thickness	Current	Flux on the central 5 mm × 5 mm area	Mean KE
3 Ti (300μm)+2 He(10 cm)	0.3 μA	1.2×10^{12} p/cm^2/s	1.0 MeV
3 Ti (200μm)+2 He(10 cm)	12.3 μA	4.2×10^{13} p/cm^2/s	7.5 MeV
3 Ti (200μm)+1 Ti(150μm) +3 He(10 cm)	6.2 μA	4.5×10^{12} p/cm^2/s	4.4 MeV
4 Ti (200μm)+3 He(10 cm)	5.4 μA	1.7×10^{13} p/cm^2/s	3.0 MeV
3 Ti (200μm)+1 Ti(250μm) +3 He(10 cm)	3.1 μA	9.2×10^{12} p/cm^2/s	1.6 MeV

75

(a) Final beam profile

(b) Final Kinetic Energy
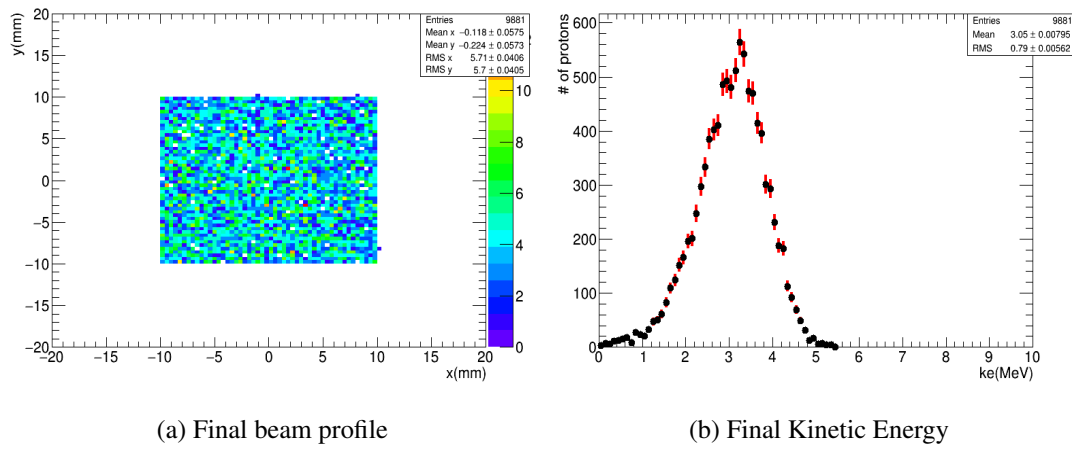
Figure 4.4: Final beam and kinetic energy distributions on the 2 cm × 2 cm zirconium sample for the METU-LEBNA project.
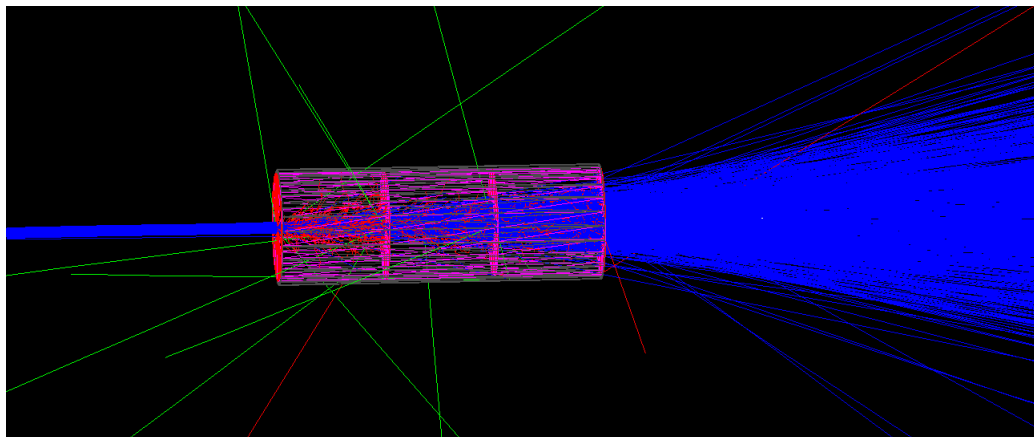
Figure 4.5: The G4beamline visual output for METU-LEBNA includes four 200 μm Ti foils and 10 cm helium cooling sections between foils. In this output, 1000 protons represented by blue is sent from the left and secondary particles are shown. A green line represent a neutron created by the foils and a red line is an electron produced by the helium sections.

Figure 4.6: The 3D drawing of the energy degradation system for the METU-LEBNA project. It has four titanium foils with 200 μm thickness and three helium sections with the length of 10 cm between them.

CHAPTER 5

CONCLUSION

In this thesis, first, the IMECE satellite and its orbital parameters, are necessary to analyse space radiation environment encountered by the IMECE are introduced. Natural radiation sources such as galactic cosmic radiation, solar particle events and trapped radiation are studied, in order to deeply understand the radiation environment. After the classification of satellite altitudes and orbits, specifically LEO radiation environment is examined because the IMECE satellite will be in such an orbit. By entering the planned orbit parameters of the IMECE satellite, SPENVIS software is used to predict the space radiation environment of the IMECE. Flux and energy distributions of trapped protons and electrons are obtained from SPENVIS and later they are examined.

Interaction of particles with matter is studied to understand how space radiation can affect a component, a device or a material. Thorough understanding of these processes are vital for the successful operation of a satellite through its expected mission duration. Three main radiation effects; namely single event effects, total ionizing dose (TID) effects and displacement damage are described in detail. TID analysis for solar cells of the IMECE satellite is performed using GEANT4 software, using the trapped particle flux and energy distributions, IMECE will be exposed in its orbit. In addition, the dose deposited in a model GaAs solar cell shielded with various thicknesses of aluminium is studied with SPENVIS, and then its results are compared with predictions for solar cells of the IMECE.

Space radiation environment tests such as SEE or TID tests are defined and some common standards for these tests and their important requirements are mentioned. In

order to perform SEE tests with 30 MeV protons, a beamline is currently being constructed in the R&D room of TAEA SANAEM Proton Accelerator Facility according to the ESA-ESCC No:25100 standards. The beam parameters available in the facility and the required beam parameters in the standard are described in detail and compared. In order to obtain the desired beam parameters, the available beam in the R&D room must be enlarged with quadrupole magnets, must be scattered with foils and then collimated. By using these beam elements and collimators with variable apertures, METU-DBL is being constructed to satisfy the required beam parameters and provide users a wide range of possible tests. G4beamline simulation program is used to calculate the secondary particle production and prompt dose rate created by some beam elements and the radiation environment of the target area in detail. In addition, the preliminary studies for METU-LEBNA project are presented. For this project, a short energy degrading beamline is designed to provide the desired beam parameters for testing zirconium samples used in nuclear applications.

REFERENCES

[1] TÜBİTAK-UZAY, "İMECE." http://uzay.tubitak.gov.tr/tr/uydu-uzay/imece. Last access on 1.10.2016.

[2] W. Larson and J. Wertz, *Space Mission Analysis and Design. Second edition.* Microcosm, Inc.,Torrance, CA (US), Dec 1992.

[3] G. F. Abdelal, N. Abuelfoutouh, and A. H. Gad, *Finite Element Analysis for Satellite Structures: Applications to Their Design, Manufacture and Testingsas.* Springer Science & Business Media, 2012.

[4] 2016 Yılı Yatırım Programı, 29505 Sayılı Resmî Gazete, 2015. Last access on 23.11.2016.

[5] D. Heynderickx *et al.*, "ESA's SPace ENVironment Information System (SPEN-VIS): a WWW Interface to Models of the Space Environment and Its Effects," *Proc. AIAA*, vol. 371, 2000.

[6] S. Agostinelli *et al.*, "GEANT4—a Simulation Toolkit," *Nuclear Instruments and Methods in Physics Research Section A: Accelerators, Spectrometers, Detectors and Associated Equipment*, vol. 506, no. 3, pp. 250–303, 2003.

[7] ESA, "Single Event Effects Test Method and Guidelines, ESCC Basic Specification No. 25100", 2014.

[8] NASA Space Radiation Analysis Group, "What is Space Radiation?", https://srag.jsc.nasa.gov/spaceradiation/What/What.cfm. Last access on 1.11.2016.

[9] NASA Earth Observatory, "Three Classes of Orbit", http://earthobservatory.nasa.gov/Features/OrbitsCatalog/page2.php. Last access on 25.10.2016.

[10] T. I. Gombosi and A. Arbor, *Physics of the Space Environment.* Cambridge University Press, 1998.

[11] L. A. Andrew Holmes, *Handbook of Radiation Effects.* Oxford University press, 2007.

[12] J. Alcaraz *et al.*, "Protons in Near Earth Orbit," *Physics Letters B*, vol. 472, no. 1, pp. 215–226, 2000.

[13] M. Aguilar *et al.*, "Precision Measurement of the Proton Flux in Primary Cosmic Rays from Rigidity 1 GV to 1.8 TV with the Alpha Magnetic Spectrometer

on the International Space Station," *Physical review letters*, vol. 114, no. 17, p. 171103, 2015.

[14] J. Beatty and J. Matthews, "Cosmic Rays." http://pdg.lbl.gov/2011/reviews/rpp2011-rev-cosmic-rays.pdf, August 2011.

[15] H. E. J. Konskenin, *Physics of Space Storms from the Solar Surface to the Earth*. Praxis, 2011.

[16] ESA, "Radiation Environment." http://www.esa.int/OurActivities/Space EngineeringTechnology/SpaceEnvironment/Radiationenvironment. Last access on 28.10.2016.

[17] M. Markovic, "South Atlantic Anomaly." https://en.wikipedia.org/wiki/South AtlanticAnomaly. at English Wikipedia [Public domain].

[18] D. H. Hathaway, "Solar Cycle Forecasting," in *The Origin and Dynamics of Solar Magnetism*, pp. 401–412, Springer, 2008.

[19] "The Earth's Trapped Particle Radiation Environment", https://www.spenvis.oma.be/help/background/traprad/traprad.html #SCEFF. Last access on 28.10.2016.

[20] "Solar Cycle Effects", https://www.spenvis.oma.be/help/ background / traprad/-traprad.html#ANISO. Last access on 28.10.2016.

[21] S. L. Snowden and M. Arida, "South Atlantic Anomaly," *ROSAT Guest Observer Facility*, Retrieved October 16, 2007.

[22] E. G. Stassinopoulos, M. A. Xapsos, and C. A. Stauffer, "Forty-Year" Drift" and Change of the SAA," 2015.

[23] K. Bedingfield, R. D. Leach, *et al.*, "Spacecraft System Failures and Anomalies Attributed to the Natural Space Environment," 1996.

[24] "General Orbit Parameters." https://www.spenvis.oma.be/help/models/sapre-earth .html. Last access on 27.11.2016.

[25] W. R. Leo, *Techniques for Nuclear and Particle Physics Experiments: a How-to Approach*. Springer Science & Business Media, 2012.

[26] A. Holmes-Siedle and L. Adams, "Handbook of Radiation Effects," 1993.

[27] E. Petersen, *Single Events Effects in Aerospace*. IEEE Press, 2011.

[28] J. Lauenstein and M. Lauenstein, "Standards for Radiation Effects Testing: Ensuring Scientific Rigor in the Face of Budget Realities and Modern Device Challenges," in *The Hardened Electronics and Radiation Technology (HEART) 2015 Conference*, April 21-24, 2015.

[29] K. Label *et al.*, "Single Event Effect Criticality Analysis," *NASA Headquarters/ Code QW*, 1996.

[30] R. Gaillard, "Single Event Effects: Mechanisms and Classification," in *Soft Errors in Modern Electronic Systems*, pp. 27–54, Springer, 2011.

[31] K. A. LaBel, "Radiation Effects on Electronics 101: Simple Concepts and New Challenges," in *NEPP Webex Presentation*, Apr 21,2004.

[32] M. Alderighi *et al.*, "Long Duration Balloon Flights for the Evaluation of Radiation Effects on Electronic Systems," *Memorie della Societa Astronomica Italiana*, vol. 79, p. 883, 2008.

[33] M. Robbins, "Final Test Guideline," 16th May 2014. Displacement Damage Guideline Project.

[34] NASA, "Space Radiation Protection," Tech. Rep. NASA SP-8054, 1970.

[35] CHARM-Facility, "Radiation hardness assurance." https://lhcb-elec.web.cern. ch/lhcb-elec/html/radiation-hardness.htm, 2014. CERN, Last access on 06.12. 2016.

[36] NASA-GoddardSpaceFlightCenter, "What is Space Radiation?." https://lws-set. gsfc.nasa.gov/space-radiation.html. Last access on 20.11.2016.

[37] M. Shea *et al.*, "Spacecraft Problems in Association with Episodes of Intense Solar Activity and Related Terrestrial Phenomena During March 1991," *IEEE transactions on nuclear science*, vol. 39, no. 6, pp. 1754–1760, 1992.

[38] Personal communication, S. Özçelik, "Gazi University".

[39] Personal communication, D. Veske, "Middle East Technical University".

[40] ESA, "ECSS-E-ST-20-08C Rev.1 Photovoltaic Assemblies and Components," 18 July 2012.

[41] ISO, "ISO 23038:2006 Standard, Space Systems—Space Solar Cells—Electron and Proton Irradiation Test Methods," 2006.

[42] B. Anspaugh, "GaAs Solar Cell Radiation Handbook," 1996.

[43] TRAD, "The 3D CAD Tool For Radiation Shielding Analysis." http://www.fast rad.net/. Last access on 28.11.2016.

[44] TRAD-training, "Introduction to Dose Calculation and Shielding with FAST-RAD and Characterization of Radiation Effects on Electronics," 20-23 June 2016. Toulouse, France.

[45] Personal Communication, Z. Unal, TAEA SANAEM.

[46] R. Uzel *et al.*, eds., *In-Situ Total Ionizing Dose Tests of SSPA Components*, AM-ICSA 2016 conference proceedings, 2016.

[47] "Nuclear Science Application and Research Center." http://nukleer.akdeniz.edu.tr/nuba. Last access on 17.02.2017.

[48] PSI, "The Proton Irradiation Facility PIF." http://pif.web.psi.ch/. Last access on 02.01.2016.

[49] "IRRAD-1." https://irradiation.web.cern.ch/irradiation/irrad1.htm. Last access on 26.01.2017.

[50] "Particle Parameters." http://cyclotron.crocker.ucdavis.edu/radiations-effects/particle-parameters/. Last update: February 23, 2015.

[51] "Parameters of the Proton Beam Facility." http://www.cyc.ucl.ac.be/LIF/LIF.php. Last access on 26.01.2017.

[52] TAEK, "Proton Accelerator Facility Booklet", TAEK SANAEM, 2012.

[53] "Experimental Space Radiation and Astroparticle Physics Group", http://esrap.physics.metu.edu.tr/en/. Last access on 17.02.1017.

[54] A. Gencer *et al.*, "Defocusing beam line design for an irradiation facility at the taea sanaem proton accelerator facility," *Nuclear Instruments and Methods in Physics Research Section A: Accelerators, Spectrometers, Detectors and Associated Equipment*, vol. 824, pp. 202–203, 2016.

[55] F. Faccio, "Radiation Effects in the Electronics for CMS," *slide, CERN*, 2001.

[56] D. Kiziloren, "DESIGN OF AN IRRADIATION TEST FACILITY FOR SPACE APPLICATIONS", Master's Thesis, Middle East Technical University, 2016.

[57] Personal communication, A. Gencer, "Middle East Technical University".

[58] Personal communication, A. Avaroglu, "Middle East Technical University".

[59] IBA. http://www.iba-radiopharmasolutions.com/products/cyclotrons. Last access on 20.01.2017.

[60] T. J. Roberts, K. Beard, S. Ahmed, D. Huang, *et al.*, "G4beamline Particle Tracking in Matter Dominated Beam Lines," in *Proc. PAC*, vol. 2013, pp. 373–375, 2011.

[61] H. Barletta, Spentzouris, "Defining Emittance." Class notes for USPAS course, 2012.

[62] Y. Z. Jeff Holmes, Stuart Henderson, "Transverse Beam Optics." http://uspas.fnal.gov/materials/09VU/Lecture6.pdf, 2009. USPAS Lecture.

[63] E. Forest, *Beam Dynamics*, vol. 8. CRC Press, 1998.

[64] S. H. Jeff Holmes and Y. Zhang, "Magnetic Fields and Magnet Design." USPAS Lecture, January, 2009. Lecture notes.

[65] K. W. Mike Syphers, Alfonse Pham and D. Alt, "Beam vs. Optical Properties." USPAS Fundamentals of Particle Accelerators Lecture, 2016. Lecture Notes.

[66] D. Groom and S. Klein, "Passage of Particles through Matter," *The European Physical Journal C-Particles and Fields*, vol. 15, no. 1-4, pp. 163–173, 2000.

[67] S. Meroli, "Multiple Scattering for Particles in the Matter." http://meroli. web.cern.ch/meroli/lecture-multiple-scattering.html, 25 April 2012. Last access on 10.12.2016.

[68] K. L. Brown, F. Rothacker, D. C. Carey, and F. C. Iselin, "Transport," tech. rep., SLAC-91-REV-2, 1973.

[69] U. Rohrer, "PSI Graphic Turtle Framework based on a CERN-SLAC-FERMI-LAB version by KL Brown et al," *URL http://people.web.psi.ch/ rohrer_u/turtle. htm*, 2007.

[70] B. Stroustrup, *The C++ Programming Language*. Pearson Education, India, 1995.

[71] W. Joho, *Representation of Beam Ellipses for Transport Calculations*. Schweizerisches Institut für Nuklearforschung, 1980.

[72] T. Roberts, "G4beamline User's Guide," *Muons Inc*, 2012.

[73] T. Nakamura and L. Heilbronn, *Handbook on Secondary Particle Production and Transport by High-Energy Heavy Ions*. World Scientific, 2006.

[74] C. Patrignani *et al.*, "Review of Particle Physics," *Chin. Phys.*, vol. C4, no. 10, p. 100001, 2016.

[75] V. Vylet, "Prompt Radiation Fields at Accelerators." http://hpschapters.org/ sections/accelerator/PDS/3PromptRad-Vylet.pdf, 2008. Last access on 10.12. 2016.

[76] S. J. Zinkle and J. T. Busby, "Structural Materials for Fission & Fusion Energy," *Materials Today*, vol. 12, no. 11, pp. 12–19, 2009.

[77] R. Ewing, W. Weber, and F. Clinard, "Radiation Effects in Nuclear Waste Forms for High-Level Radioactive Waste," *Progress in Nuclear Energy*, vol. 29, no. 2, pp. 63–127, 1995.

[78] W. J. Weber, "Irradiation Effects in Materials for Nuclear Applications," in *EPJ Web of Conferences*, vol. 51, p. 02001, EDP Sciences, 2013.

[79] S. Nanikawa, Y. Eto, and S. Shimada, "Zirconium Alloy for Nuclear Reactors," 1997.

[80] G. Audi, O. Bersillon, *et al.*, "The NUBASE Evaluation of Nuclear and Decay Properties," *Nuclear Physics A*, vol. 624, no. 1, pp. 1–124, 1997.

[81] J. Kopecky *et al.*, "Atlas of Neutron Capture Cross Sections," *International Nuclear Data Committee*, 1997.